

AN ABSTRACT OF THE THESIS OF

Matthew S. Segrin for the degree of Master of Science in Atmospheric Sciences  
presented on June 14, 2006.

Title: Using Ship Tracks to Characterize the Effects of Haze on Cloud Properties.

Abstract approved:

---

James A. Coakley, Jr.

1-km MODIS observations of ship tracks off the west coast of the U.S. are used to characterize changes in cloud visible optical depths, cloud droplet radii, cloud cover fraction, and column cloud liquid water amount as low-level marine clouds respond to particle pollution from underlying ships. This study re-examines the finding of earlier studies based on Advanced Very High Resolution Radiometer (AVHRR) observations showing that when restricted to pixels overcast by low-level, single-layered cloud systems, the polluted clouds in the ship tracks had on average ~20% less liquid water than the nearby uncontaminated clouds. This study uses Moderate Imaging Spectroradiometer (MODIS) observations from the *Terra* and *Aqua* satellites and takes advantage of the 1.6 and 2.1- $\mu\text{m}$  channels in addition to the 3.7- $\mu\text{m}$  channel available on AVHRR to derive droplet effective radii. The additional channels allow for different and presumably more comprehensive analyses of the cloud properties. In

addition, this study uses a retrieval scheme that accounts for the effects of partial cloudiness within the 1-km pixels on the retrieved cloud properties. An improved automated track finding scheme that allows for the selection of unpolluted clouds to be closer to the clouds identified as being polluted is also employed in this study. When restricted to overcast pixels, as was done in earlier studies, results from the *Terra* and *Aqua* MODIS observations indicate that cloud droplet effective radii are significantly smaller and cloud optical depths significantly larger for polluted pixels than for unpolluted pixels. Cloud top height does not change when clouds become polluted but cloud liquid water path decreases slightly but significantly. The decrease in cloud liquid water obtained with the MODIS observations was at most ~10%, much less than the 20% obtained with the AVHRR observations. This decrease, however, depended on the wavelength used to derive the droplet effective radii. Also, the clouds that were most sensitive to pollution were those with small optical depths and large droplet effective radii.

© Copyright by Matthew S. Segrin

June 14, 2006

All Rights Reserved

Using Ship Tracks to Characterize the Effects of Haze on Cloud Properties

by

Matthew S. Segrin

A THESIS

submitted to

Oregon State University

in partial fulfillment of  
the requirements for the  
degree of

Master of Science

Presented June 14, 2006

Commencement June 2007

Master of Science thesis of Matthew S. Segrin presented on June 14, 2006.

APPROVED:

---

Major Professor, representing Atmospheric Sciences

---

Dean of the College of Oceanic and Atmospheric Sciences

---

Dean of the Graduate School

I understand that my thesis will become part of the permanent collection of Oregon State University libraries. My signature below authorizes release of my thesis to any reader upon request.

---

Matthew S. Segrin, Author

## ACKNOWLEDGEMENTS

I would like to express my sincere thanks to Professor James A. Coakley, Jr., for the chance to work under his guidance and leadership. His passion for science and knowledge was always encouraging. Coming to Oregon State University I did not have any financial support until Professor Coakley gave me the opportunity to work with him. Support for this work was through NASA Grant NNG04GF42G.

I would also like to thank Bill Tahnk and Mark Matheson for all the help and advice they gave me. The support, patience and knowledge they showed me were invaluable. Thanks also to my fellow students who made classes and the lab more enjoyable.

I wish to thank Drs. Rick Vong, Cindy Twohy, and Ron Doel for examining my thesis and serving on my committee.

Thanks to my parents, grandparents, siblings, and in-laws for all your support and prayers. Without you guys this thesis would not have been possible.

I especially would like to thank my wife, Katherine Segrin. Without her encouragement, patience, compassion and support I would not have made it through the process.

## TABLE OF CONTENTS

	<u>Page</u>
Chapter 1: Introduction .....	1
1.1 Motivation .....	1
1.2 Background .....	4
1.3 Outline of Thesis .....	8
Chapter 2: Data Analysis .....	10
Chapter 3: Ship Track Results .....	18
3.1 <i>Terra</i> Observations .....	18
3.2 <i>Aqua</i> Observations .....	42
3.3 Comparing <i>Terra</i> Observations with <i>Aqua</i> Observations .....	64
3.4 Statistical Independence .....	66
Chapter 4: Cloud Sensitivity .....	70
Chapter 5: Conclusions .....	80
Bibliography .....	83
Appendix: Automated scheme for identifying ship tracks .....	86

## LIST OF FIGURES

<u>Figure</u>		<u>Page</u>
2.1	Image of ship track created from a) 0.64- $\mu\text{m}$ reflectances, b) and c) 2.1- $\mu\text{m}$ reflectances, and d) 3.7- $\mu\text{m}$ radiances. . . . .	14
2.2	Ship track locations for <i>Terra</i> (2001 – 2003). . . . .	15
2.3	Ship track locations for <i>Aqua</i> (2002 – 2004). . . . .	16
3.1	Cloud optical depths for the ship track pixels (solid black line), control 1 pixels (dotted blue line), and the control 2 pixels (dashed red line) taken from 20-pixel track segments. . . . .	27
3.2	Same as figure 3.1 except for droplet effective radius derived using the 3.7- $\mu\text{m}$ channel. . . . .	28
3.3	Same as figure 3.1 except for liquid water path derived using the 3.7- $\mu\text{m}$ channel. . . . .	29
3.4	Same as figure 3.1 except for droplet effective radii and cloud liquid water paths derived using the 1.6 and 2.1- $\mu\text{m}$ channels. . . . .	30
3.5	Average distance and the distance-weighted bearings. . . . .	33
3.6	Mean differences between the ship and controls (solid blue line) and between control 1 and control 2 (dashed red line) for cloud optical depth, droplet effective radii derived using the 1.6, 2.1 and 3.7- $\mu\text{m}$ channels, and the associated cloud liquid water paths, taken from 20-pixel track segments. . . . .	34
3.7	Distribution a) shows the average cloud top height for the ship track pixels (solid black line), control 1 pixels (dotted blue line), and the control 2 pixels (dashed red line) taken from 20-pixel track segments. . . . .	38
3.8	Cloud optical depths for the ship track pixels (solid black line), control 1 pixels (dotted blue line), and the control 2 pixels (dashed red line) taken from 20-pixel track segments. . . . .	49
3.9	Same as figure 3.8 except for droplet effective radii derived using the 3.7- $\mu\text{m}$ channel. . . . .	50
3.10	Same as figure 3.8 except for liquid water path derived using the 3.7- $\mu\text{m}$ channel. . . . .	51

## LIST OF FIGURES (Continued)

<u>Figure</u>	<u>Page</u>
3.11	Same as figure 3.8 except for droplet effective radii and cloud liquid water paths derived using the 1.6 and 2.1- $\mu\text{m}$ channels. . . . . 52
3.12	Average distance and the distance-weighted bearings. . . . . 55
3.13	Mean differences between the ship and controls (solid blue line) and between control 1 and control 2 (dashed red line) for cloud optical depth, droplet effective radii derived using the 1.6, 2.1 and 3.7- $\mu\text{m}$ channels, and the associated cloud liquid water paths, for 20-pixel track segments. . . . . 56
3.14	Same as figure 3.7 except for <i>Aqua</i> observations. . . . . 60
4.1	Distribution of changes in reflectance for <i>Terra</i> and <i>Aqua</i> observations. . . 74
4.2	Change in cloud reflectance and fractional change in cloud optical depth. . 75
4.3	Fractional change in optical depth for droplet effective radii and cloud optical depths associated with the control pixels. . . . . 76
4.4	Same as figure 4.3 except for <i>Aqua</i> observations. . . . . 77
4.5	Changes in cloud liquid water paths for droplet effective radii and cloud optical depths associated with the control pixels. . . . . 78
4.6	Same as figure 4.5 except for <i>Aqua</i> observations. . . . . 79
A1	Image of ship track created from 2.1- $\mu\text{m}$ reflectances a), droplet effective radius retrieved using the 2.1- $\mu\text{m}$ reflectances b), and method for identifying pixels containing polluted clouds c). . . . . 83

## LIST OF TABLES

<u>Table</u>	<u>Page</u>
2.1 Ship tracks analyzed. . . . .	17
3.1 Means and standard deviation of the means for cloud optical depths, cloud droplet effective radii derived using the 1.6, 2.1, and 3.7- $\mu\text{m}$ channels, and the associated cloud liquid water paths for the ship track and controls. . . .	31
3.2 Means and standard error of the means for the differences between ship and controls and the differences between control 1 and control 2 for cloud optical depths, cloud droplet effective radii derived using the 1.6, 2.1, and 3.7- $\mu\text{m}$ channels, and the associated cloud liquid water paths. . . . .	32
3.3 Means for the differences between ship and controls along with the 99% confidence intervals for each of the cloud properties. . . . .	36
3.4 Means and standard error of the means for the differences between ship and controls and the randomized differences between control 1 and control 2 for cloud optical depth, cloud droplet effective radius derived using the 1.6, 2.1, and 3.7- $\mu\text{m}$ channels, and the associated cloud liquid water paths. . . . .	37
3.5 Same as Table 3.1 except segments were kept only if they had changes in cloud droplet effective radii that were greater than or equal to 2 $\mu\text{m}$ . . . . .	39
3.6 Means and standard error of the means for differences between ship and controls and randomized differences between control 1 and control 2 for droplet effective radii derived using the 1.6, 2.1 and 3.7- $\mu\text{m}$ channels, cloud optical depths, and cloud liquid water paths. . . . .	40
3.7 Same as Table 3.3 except segments were kept only if they had changes in cloud droplet effective radii that were greater than or equal to 2 $\mu\text{m}$ . . . . .	41
3.8 Means and standard deviation of the means for cloud optical depths, cloud droplet effective radii derived using the 1.6, 2.1, and 3.7- $\mu\text{m}$ channels, and the associated cloud liquid water paths for the ship track and controls. . . .	53
3.9 Means and standard error of the means for the differences between ship and controls and the differences between control 1 and control 2 for cloud optical depths, cloud droplet effective radii derived using the 1.6, 2.1, and 3.7- $\mu\text{m}$ channels, and the associated cloud liquid water paths. . . . .	54
3.10 Means for the differences between ship and controls along with the 99% confidence intervals for each of the cloud properties. . . . .	58

LIST OF TABLES (Continued)

<u>Table</u>	<u>Page</u>
3.11 Means and standard error of the means for the differences between ship and controls and the randomized differences between control 1 and control 2 for cloud optical depths, cloud droplet effective radii derived using the 1.6, 2.1, and 3.7- $\mu\text{m}$ channels, and the associated cloud liquid water paths. . . . .	59
3.12 Same as Table 3.6 except segments were kept only if they had changes in the droplet effective radii that were greater than or equal to 2 $\mu\text{m}$ . . . . .	61
3.13 Same as Table 3.5 except for <i>Aqua</i> observations. . . . .	62
3.14 Same as Table 10 except segments were kept only if they had changes in cloud droplet effective radii that were greater than or equal to 2 $\mu\text{m}$ . . . . .	63
3.15 Same as table 3.1 except there was at least a 20-pixel separation measured along the ship track between the segments, and of the remaining segments a third were randomly chosen to be analyzed. . . . .	69
3.16 Same as table 3.6 except there was at least a 20-pixel separation measured along the ship track between the segments, and of the remaining segments a third were randomly chosen to be analyzed. . . . .	69

# USING SHIP TRACKS TO CHARACTERIZE THE EFFECTS OF HAZE ON CLOUD PROPERTIES

## CHAPTER 1

### INTRODUCTION

#### 1.1 Motivation

Changes in aerosols are expected to have a significant effect on the Earth's climate. Aerosols scatter and absorb sunlight and terrestrial radiation thereby affecting the Earth's energy budget. This interaction of aerosols with radiation is referred to as the direct effect. Aerosols cause a net increase in Earth's albedo, the portion of sunlight reflected back to space (IPCC 2001). Aerosols also influence the climate through their ability to change droplet numbers and sizes, thereby changing the effect of clouds on the Earth's radiation budget. The effect of aerosols on the climate through changes in cloud properties is referred to as the aerosol indirect effect. The magnitude of the aerosol indirect effect is one of the largest uncertainties in assessments of the anthropogenic forcing of climate (IPCC 2001). The large uncertainty is partly due to poor knowledge of how particles affect clouds and partly due to an inability to model clouds in the climate system.

Aerosols, both anthropogenic and natural, can act as cloud condensation nuclei (CCN) on which cloud droplets form. The number of available CCN is one parameter that helps to determine the cloud droplet number concentration, and thus cloud albedo and precipitation formation (Lohmann and Feichter 1997). For fixed liquid water, an increase in CCN leads to an increase in droplet numbers but the droplets are smaller.

This change in droplet number and size is referred to as the Twomey effect, or the “first indirect effect” of aerosols (Twomey 1974). With fixed liquid water amount, the increase in droplet number causes an increase in cloud reflectivity even though the droplets are smaller. Such changes would therefore contribute to the cooling of the Earth. The “second aerosol indirect effect,” also known as the “cloud lifetime effect,” is the suppression of precipitation that results from the smaller droplet sizes. The suppression of precipitation is thought to cause a significant increase in the liquid water content of the cloud and also increase cloud lifetimes (Albrecht 1989). Albrecht (1989) points out that the formation of precipitation by collision and coalescence does not occur as readily in clouds that have small droplets. Clouds with high cloud droplet number concentration have smaller mean droplet sizes and narrower droplet size spectra. Consequently, precipitation is less likely to occur within a polluted cloud.

Ship tracks offer one of the most direct ways in which the response of clouds to particle pollution can be studied. Ship tracks are narrow lines of perturbed regions in marine stratiform (stratus and stratocumulus) clouds, caused by smoke stack plumes from underlying ships. The tracks show up particularly well as lines of enhanced reflectance at near infrared wavelengths (Coakley et al. 1987). Ship tracks can also appear as narrow lines of clouds in a seemingly cloud-free sky (Conover 1966). Hobbs et al. (2000) characterize ship tracks as being long-lived, linear regions of enhanced solar reflectivity in marine stratiform clouds that appear in satellite imagery downwind of ships. The tracks provide a means of studying the changes in cloud properties that arise because of the pollution. Polluted clouds can be compared

directly with nearby unpolluted clouds to measure the differences due solely to the pollution.

Using a different methodology but nearly identical criteria, one goal of this study was to attempt replicating the results of a previous study done by Coakley and Walsh (2002). The Coakley and Walsh study also used satellite observations of ship tracks to determine how clouds responded when haze was added. They found that clouds polluted by underlying ships displayed reflectivities that were generally higher at visible wavelengths, but that this change was difficult to detect. They also found that the droplet effective radii in these clouds were smaller, and cloud liquid water remained constant. When they looked at clouds that produced the largest changes in droplet effective radii, however, they found a statistically significant enhancement in cloud reflectivity and a significant reduction in cloud liquid water. Being able to replicate the results of the Coakley and Walsh study would help answer the question of whether or not the results they obtained were reliable.

Another goal of this study was to check the assumption that the samples analyzed were statistically independent. In this study, logged ship tracks were broken into 20-pixel segments along the track. The segments were then tested against a number of criteria, and those segments that passed the criteria were what made up the samples and were then analyzed. Verifying statistical independence is required to assure the validity of the estimates of statistical uncertainty. Yet another goal was to determine the sensitivity of clouds to pollution by underlying ships. Cloud sensitivity is directly related to cloud susceptibility as describe by Platnick and Twomey (1994). Furthermore, a deeper look into which clouds demonstrated the most sensitivity to

changes in cloud albedo and why these particular clouds showed the most change was investigated.

## 1.2 Background

1-km resolution Moderate Resolution Imaging Spectroradiometer (MODIS) imagery collected from *Terra* and *Aqua* satellites distinctly show ship tracks at all wavelengths when ships spawn clouds in otherwise cloud-free or partly cloudy regions. Ship tracks in the near-infrared wavelengths, however, show up even in regions overcast by clouds whereas at 0.64  $\mu\text{m}$  they are lost in the variability of reflectivities typically exhibited by marine stratus. There are many reasons why ship tracks show up more clearly at 3.7  $\mu\text{m}$  than at 0.64  $\mu\text{m}$ . At 3.7  $\mu\text{m}$  water droplets both absorb and scatter solar radiation (Platnick et al. 2000). Coakley et al. (1987) report that the scattering cross section of a droplet is approximately proportional to its geometric cross section, while the absorption cross section is approximately proportional to the droplet's volume. Because of this relationship, the ratio of scattering to absorption increases as the droplet radius decreases. Therefore, as droplet radii decrease, there is additional scattering that leads to an increase in cloud reflectivity. The enhanced radiances at 3.7  $\mu\text{m}$  that identify ship tracks are taken to be the result of cloud droplets shifting to smaller sizes. Furthermore, at 0.64  $\mu\text{m}$ , liquid water is nonabsorbing and the cross section of a cloud droplet is approximately proportional to its geometric cross section. Thus, the amount of scattering in the cloud and the total cloud reflectivity would increase as droplet number increases (Coakley et al. 1987). Droplet numbers, however, are highly variable in comparison with droplet

radii. Consequently, as Platnick et al. (2000) point out, the 3.7- $\mu\text{m}$  band is expected to have a change in reflectance that is a factor of two to six times greater than the change for visible channels.

Ship tracks form in stratiform clouds that are several hundred meters thick located near the top of the marine boundary layer. Classifying the type of emissions from ships is one way to evaluate the effect emissions have on clouds. Under the same ambient conditions, some ships produce tracks while others do not. To better understand the formation of ship tracks the Monterey Area Ship Track (MAST) experiment was conducted off the coast of California in June 1994. Aircraft collected in situ measurements of ship stack emissions and their effects on clouds (Durkee et al. 2000). Hobbs et al. (2000) found that if emissions from ships were responsible for ship tracks, then it could be expected that for the same ambient conditions, a ship powered by a low-grade fuel would be more likely to produce ship tracks than a ship powered by a high-grade distillate fuel. Compared to ships burning high-grade distillate fuel, ships burning low-grade fuel emit a greater number of particles large enough to serve as cloud condensation nuclei. Hobbs et al. (2000) also found that diesel-powered and steam turbine-powered ships burning navy distillate fuels emitted from  $\sim 4 \times 10^{15}$  to  $2 \times 10^{16}$  total particles per kilogram of fuel burned. Most of the particles emitted were less than 0.1  $\mu\text{m}$  in radius, with an average between  $\sim 0.01$  and 0.1  $\mu\text{m}$  (mode radius  $\sim 0.02$   $\mu\text{m}$ ). Diesel-powered ships burning marine fuel oil emitted particles with larger mode radii averaging  $\sim 0.03$ - $0.05$   $\mu\text{m}$ . The dominating factor in determining particle emissions is evidently fuel type. Ships burning low-

grade fuels, such as marine fuel oil, are more likely to produce ship tracks than ships burning higher-grade distillate fuels.

Albrecht (1989) suggested that smaller mean droplet sizes resulting from increased cloud droplet concentrations in ship tracks should result in less drizzle because droplet collisions are reduced. Suppression of drizzle may lead to an increase in liquid water content in the cloud droplet size range of ship tracks because drizzle is a sink for cloud liquid water (Ferek et al. 2000). If drizzle is suppressed in clouds that are polluted, then polluted clouds may precipitate less than unpolluted clouds. This suppression of drizzle by the polluted clouds may increase the amount and stability of stratus clouds, increasing their cooling of the climate (Ferek et al. 2000).

Ferek et al. (2000) predicted drizzle would decrease in ship tracks because the cloud droplets were smaller in the tracks and collided less frequently. They also predicted that liquid water would increase due to the decrease in drizzle. From *in situ* measurements, they found an increase in cloud droplet number concentration and a decrease in cloud droplet size in the clouds where ship tracks were formed. Be that as it may, an increase in liquid water content was not always observed in the ship tracks. The effect of ship exhaust on drizzle depends on several boundary layer factors, particularly aerosol loading in ambient air and stability of the boundary layer. Nevertheless, under the right conditions, drizzle may be suppressed in ship tracks (Ferek et al. 2000). In contrast to the suggestions of Albrecht (1989) and the findings of Ferek et al. (2000), a study done by Coakley and Walsh (2002) found that cloud liquid water decreased in clouds that were polluted by underlying ships.

Whether ship tracks can form in clouds that are polluted or semi-polluted has been questioned. Noone et al. (2000a) found that anthropogenic emissions of aerosols can have an influence on the radiative properties of clouds in the near infrared and not necessarily in the visible. In a similar study, Noone et al. (2000b) found that one ship produced a track in satellite imagery while another ship did not. The clouds in both cases were in the same moderately polluted air mass. They concluded that the difference between the ships was based on the type of fuel the ships were burning. One ship was burning a low-grade diesel fuel while the other ship was not. Durkee et al. (2000) claim that clean, shallow boundary layers have a higher likelihood of being perturbed by the addition of ship emissions. This leads to the conclusion that ship tracks are more prolific, tending to have stronger albedos when pollution is low in the ambient marine boundary layer.

Ackerman et al. (1995) report that cloud liquid water does not always increase when the average cloud droplet size decreases. Furthermore, much of the uncertainty in the magnitude of the aerosol indirect effect comes from an inadequate understanding of the response of cloud water to changes in aerosol and cloud droplet concentrations (Ackerman et al. 2004). Using a large eddy simulation model, Ackerman et al. (2004) determined that relative humidity above the boundary layer was a leading factor in determining how cloud liquid water responds to changes in droplet concentrations. When the air above the boundary layer is moist, cloud water increases and alternatively when the air above the boundary layer is dry, there is a reduction in cloud liquid water and the aerosol indirect effect is diminished. Their

findings suggest that climate models tend to overestimate the aerosol indirect effect as most of the models produce clouds with higher liquid water amounts when polluted.

In a study done by Matheson et al. (2005), aerosol and cloud property relationships for summertime stratiform clouds in the northeastern Atlantic were investigated. They found that air in coastal regions was more polluted than air in the open ocean. Consequently, for single-layered, low-level clouds, droplet effective radii near the coast were smaller and over the open ocean they were larger. Additionally, they found that aerosol optical depth and cloud optical depth was smaller over the open ocean and larger near the coast. Furthermore, they noted that cloud liquid water path decreased as aerosol burden increased for clouds near the coast. They suggested that gradients within the clouds going from the open ocean to the coast was partly due to the mixing of dry continental air and partly due to the pollution plumes from major urban centers.

### **1.3 Outline of Thesis**

This thesis presents the results of the effects of haze particles on clouds as deduced for ship tracks. This study makes use of satellite data from MODIS. Using MODIS is advantageous because data will be collected from two separate satellites, *Terra*, a morning satellite, and *Aqua*, an afternoon satellite. Moreover, the 1.6, 2.1 and 3.7- $\mu\text{m}$  channels on the *Terra* and *Aqua* satellites are used to derive droplet effective radii which allow for different and presumably more comprehensive analyses of cloud properties. Chapter 2 reviews the analysis method for identifying and analyzing ship tracks. A summary of the *Terra* and *Aqua* observations on how cloud properties

changed when haze was added is presented in chapter 3. Also presented in chapter 3 are a comparison of the results from the *Terra* and *Aqua* observations, and a check to see if the samples in this study were statistically independent. Chapter 4 explores the concept of cloud sensitivity and why some clouds are more sensitive to change than others. A conclusion and summary of the thesis and its findings is then presented in Chapter 5.

## CHAPTER 2

### DATA ANALYSIS

A semi-automated track finding scheme was used to identify portions of the cloud polluted by underlying ships. This scheme also selected nearby unpolluted clouds so that they were close to the clouds identified as being polluted. The first step in identifying a ship track was done by hand. Satellite images at 2.1, 3.7 and 11  $\mu\text{m}$  were used to locate the ship track. The 11- $\mu\text{m}$  imagery was used to identify single-layered, low-level cloud systems, and the 2.1 and 3.7- $\mu\text{m}$  images were used to identify the ship track itself. The images were taken from *Terra* and *Aqua* satellites and were individually inspected for ship tracks by looking at each pass over the desired region,  $20^{\circ} - 45^{\circ}$  N and  $110^{\circ} - 140^{\circ}$  W. The criterion used to log the tracks was the same as that used by Coakley and Walsh (2002). The relative scan spot and scan line number within the pass were logged along the track for each individual ship track. The number of points logged varied from as little as two, to as many as ten to twenty. The number of bends within the track and the length of the track dictated the number of points logged. The first point logged was the point thought to be closest to the ship. Figure 2.1 shows an example of a logged track. The first point is referred to as the head. Only tracks that had a distinct, well-defined head were logged and analyzed. Requiring a track to have a clearly discernable head reduced the risk of logging false tracks. Track-like features occasionally appeared in the imagery and were thought to be a result of gravity waves propagating in the boundary layer. In addition, the head is

a key point because distances measured from the head of the track can be used as a measure of the time elapsed since the track was generated.

Figure 2.1 shows an example of a ship track with the positions logged by hand. The figure shows images created from reflectances at 0.64 and 2.1  $\mu\text{m}$  and radiances at 3.7  $\mu\text{m}$ . The logged points were used by the automated track-finding scheme to establish the location of the track and the domain of 2.1  $\mu\text{m}$  radiances to be analyzed. The analysis domain was typically 25 pixels perpendicular to the hand-located center of the track. The pixels that are colored are those that were selected by the automated track finding routine as the polluted pixels (red), and on either side of the track, control 1 pixels (blue) and control 2 pixels (green). Figures 2.2 and 2.3 show all of the logged positions of the ship tracks. Statistics for each ship track segment were kept if the segment fell within the region outlined in red. Figure 2.2 shows the locations of the ship tracks for *Terra*, May – August 2001 – 2003, and Figure 2.3 shows the locations for *Aqua*, June – August 2002 and May – August 2003 – 2004. The scheme for retrieving cloud properties, cloud droplet effective radius, cloud optical depth, cloud altitude, and cloud liquid water path, was the partly cloudy pixel retrieval scheme described by Coakley et al. (2005).

In a previous study (Coakley and Walsh 2002), pixels that were selected as controls were required to be at least 10 km away from any polluted pixels. For this study, however, control pixels were selected to be within as little as one pixel away from the polluted pixels. The proximity reduces somewhat the uncertainty that results from the natural variability observed for the clouds. Before comparing the properties for the polluted and unpolluted clouds, certain criteria were followed. First, each ship

track was separated into 20-pixel segments measured along the position of the track and statistics of the cloud properties for the polluted and unpolluted clouds were kept for each segment. For comparison with the earlier Coakley and Walsh (2002) study, each segment was required to contain nothing but overcast pixels for both the controls and polluted clouds. In addition, to be considered for further analysis each segment had to yield at least 20 ship track pixels and 20 control pixels on both sides of the track. Segments that lacked sufficient numbers of pixels were removed from further analysis.

The last step in the selection of track segments for analysis was a visual examination. The examination screened cases in which the automated scheme clearly failed. The failures generally occurred when multiple tracks occurred near each other and the track identification scheme picked up both tracks instead of one. Also, analysis near the edges of the images often failed. In some cases ship track segments from one ship happened to overlap those of another track, as occurred at ship track crossings and when the tracks were in close proximity to each other. In such cases the control pixels, or polluted pixels, for one track sometimes fell on the polluted pixels of another track. These crossing and overlapping segments were removed from further analysis.

Table 2.1 gives the number of ship tracks logged for the *Terra* and *Aqua* satellites. Also shown in the table is the number of tracks that were probed for the analysis, the total number of segments that fit the criteria for analysis, and the number of completely overcast segments that were analyzed for this study. Some of the logged tracks fell outside of the geographic region chosen for this study. Likewise,

segments with pixels within the region subject to sun glint, specular reflection from a flat surface, were not analyzed. Of the segments available for analysis, those that were overcast constituted approximately 10% of the total number of segments processed for *Terra*, and 13 % of the total number processed for *Aqua*.

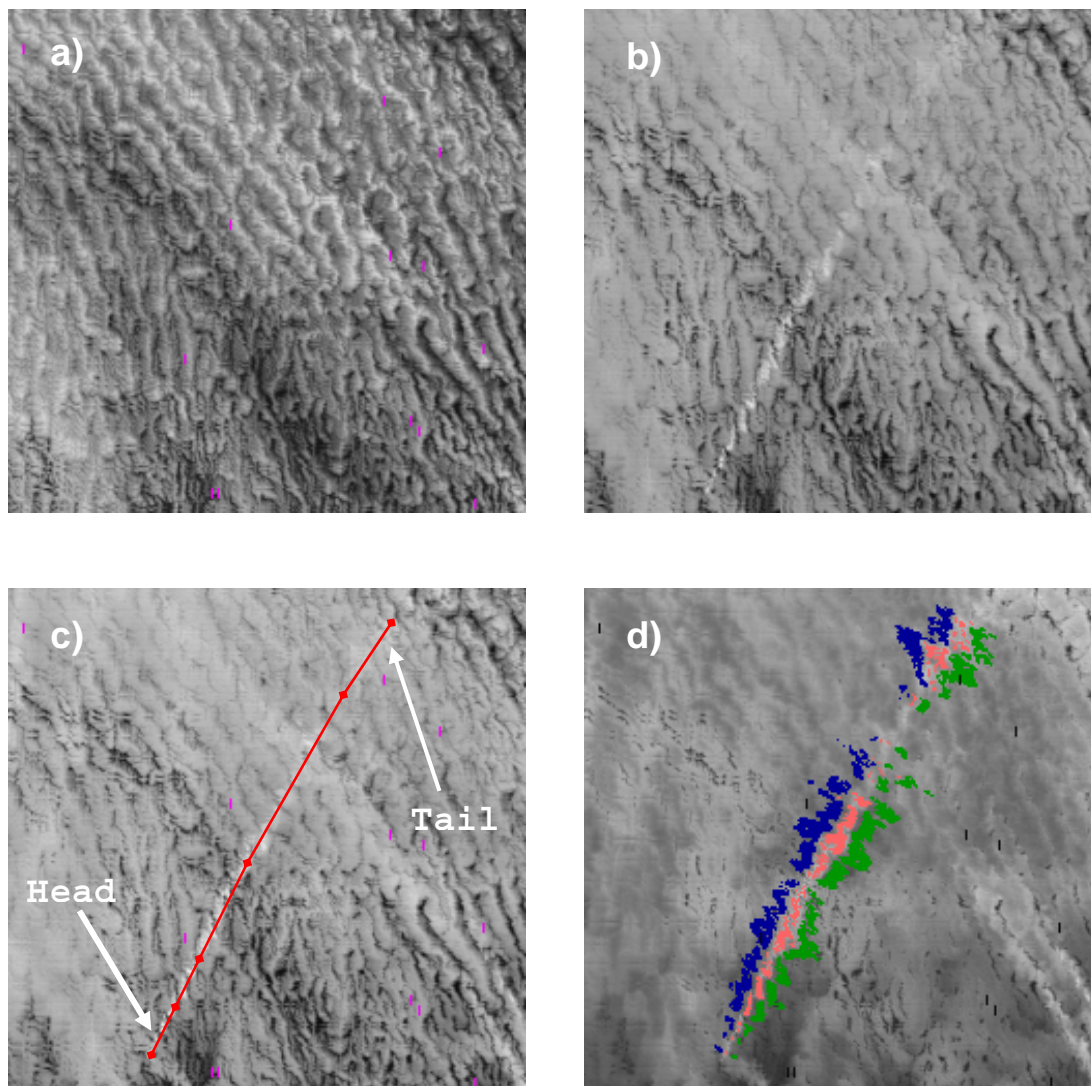


FIGURE 2.1. Image of ship track created from a) 0.64- $\mu\text{m}$  reflectances, b) and c) 2.1- $\mu\text{m}$  reflectances, and d) 3.7- $\mu\text{m}$  radiances. The points and lines in c) represent the hand-logged location of the ship track with the head and tail labeled. The pixels highlighted in d) show which pixels were selected as polluted and unpolluted. Blue and green represent control 1 and control 2 pixels respectively, and the red represents ship track pixels.

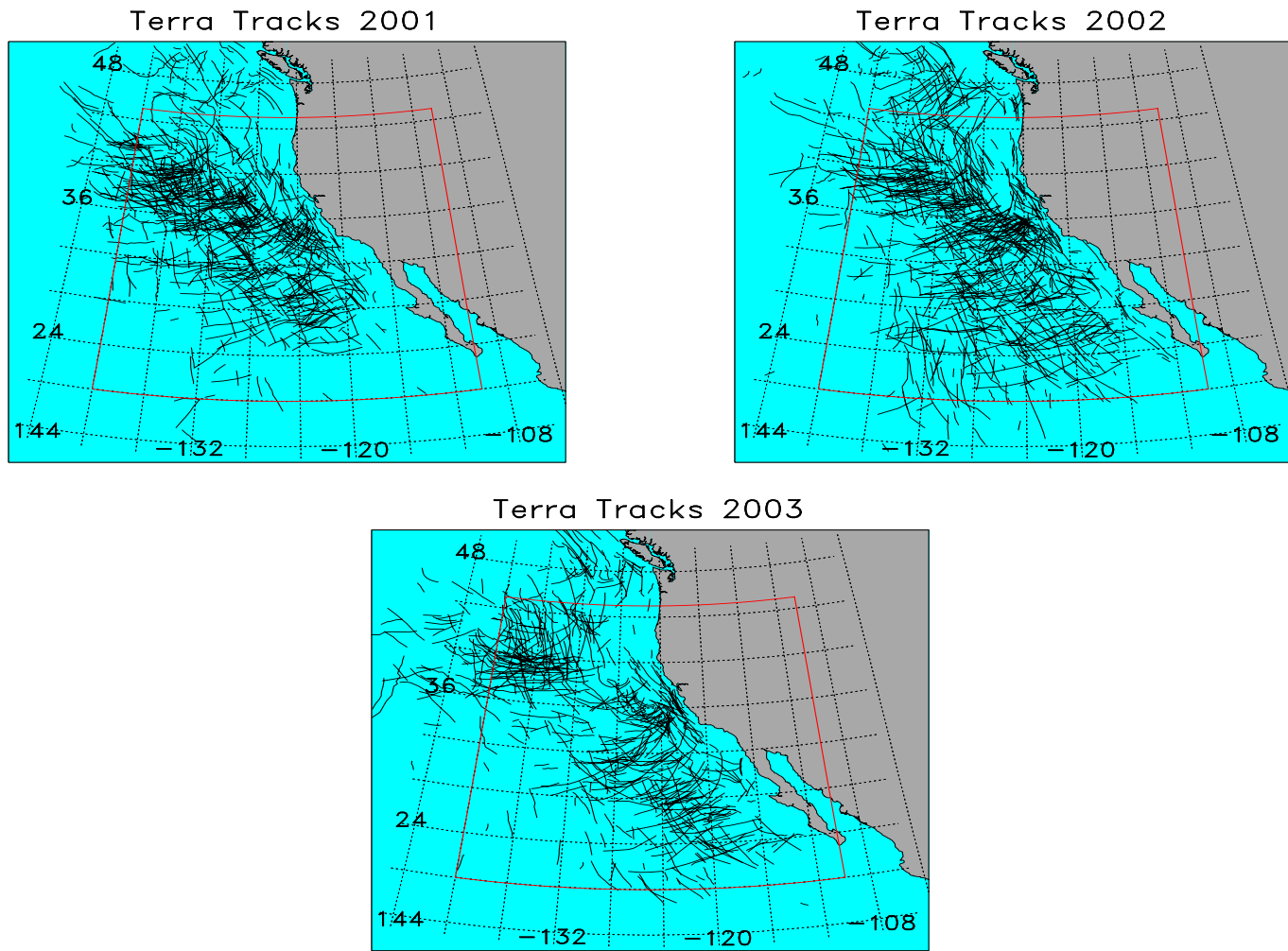


FIGURE 2.2 Ship track locations for *Terra* (2001 – 2003).

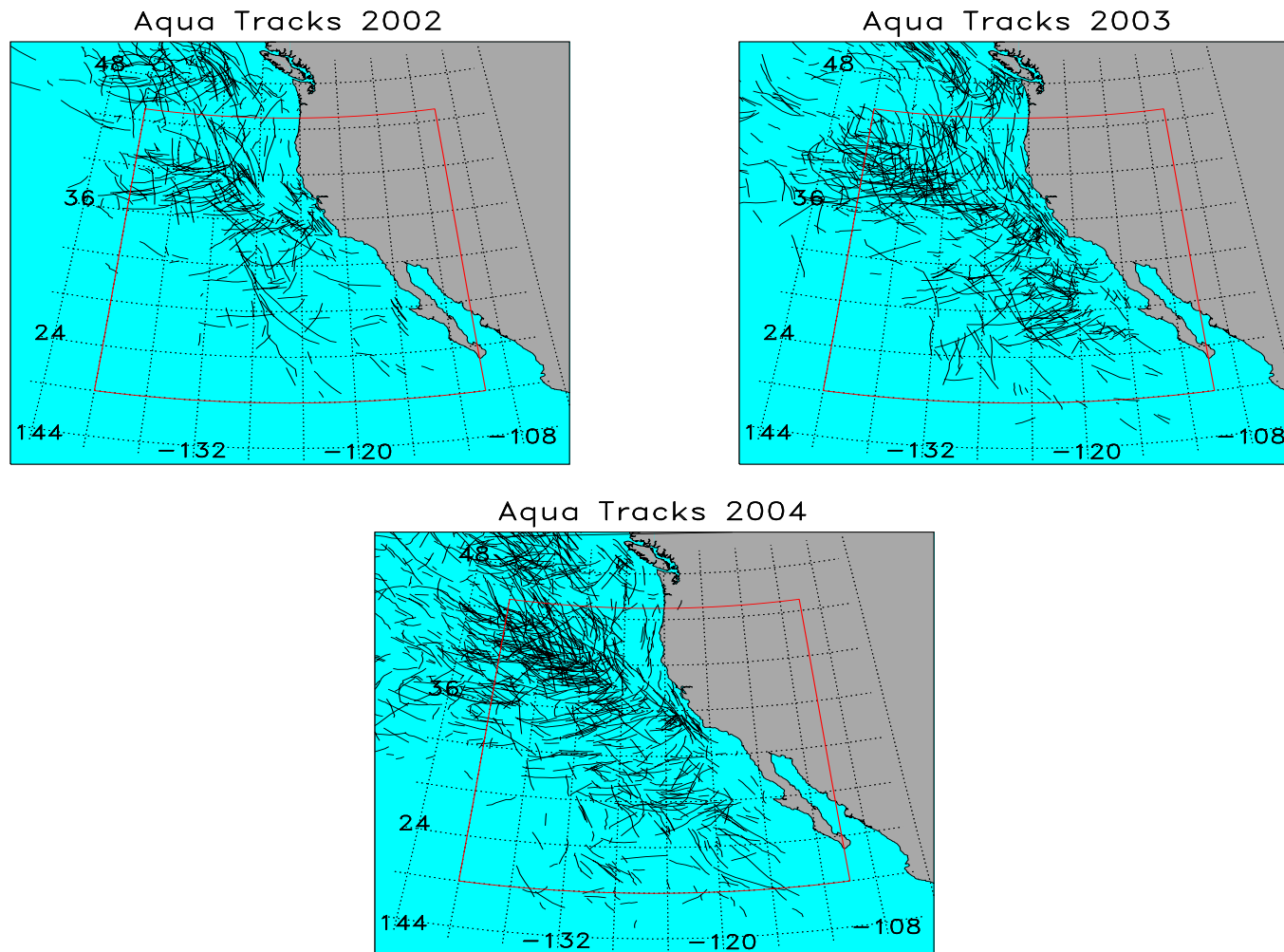


FIGURE 2.3 Ship track locations for *Aqua* (2002 – 2004).

TABLE 2.1. Ship tracks analyzed. Terra: May-August, 2001-2003. Aqua: June-August, 2002, and May-August, 2003-2004. Segments were 20-pixels along the direction of the track with the domain on either side of the track approximately equal to the combined width of the track and the controls on either side.

Satellite	Terra	Aqua
Ship tracks logged	1960	2270
Ship tracks probed for analysis	1071	990
Total number of segments processed suitable for analysis	7300	5407
Segments appropriate for completely overcast analysis	751	694

## CHAPTER 3

### SHIP TRACK RESULTS

#### 3.1 *Terra* Observations

For the *Terra* overpasses, there were 750 track segments that yielded comparisons between polluted and unpolluted clouds for the summer months May – August, 2001 – 2003. Figure 3.1 shows the distribution of optical depths for the polluted ship track pixels (solid black line) and for the pixels identified as unpolluted control 1 (dotted blue line) pixels on one side of the track and control 2 (dashed red line) pixels on the other side. Means and standard deviation of the means for the distributions of the optical depths for the ship and both controls are given. The distributions were acquired for 20-pixel segments measured along the track and total domain size on either side of the track that equaled the width of the ship track and the two controls on either side. The widths of the controls were set approximately equal to the width of the track. The means and standard deviations for the controls were essentially the same, indicating that the clouds on either side of the track were identical. The slight difference between the controls resulted from the natural variability of the clouds. Conversely, the optical depths in the ship track pixels were significantly larger compared to the control pixels. The polluted clouds have higher reflectivities than nearby unpolluted clouds. This result differs from that found by Coakley and Walsh (2002) who reported that the slight rise in optical depths for the polluted clouds was not statistically significant.

Figure 3.2 shows the distributions of droplet effective radii derived using the 3.7- $\mu\text{m}$  channel for ship track pixels (solid black line), control 1 pixels (dotted blue line), and control 2 pixels (dashed red line). Again, the means and standard deviation of the means for the distributions are given. The results in Fig. 3.2 indicate that the difference in the 3.7- $\mu\text{m}$  droplet effective radii between control 1 and control 2 pixels were in essence nonexistent. The clouds on either side of the track were identical within the uncertainty associated with the natural variability of the clouds. The ship track pixels, on the other hand, had droplet effective radii 2.6  $\mu\text{m}$  smaller than those of the control pixels. The higher concentration of cloud condensation nuclei due to the exhaust plumes of the underlying ships led to the formation of more droplets, as indicated by the rise in optical depth, but the droplets were smaller. The changes in droplet effective radii and the related changes in the 3.7- $\mu\text{m}$  radiances were, of course, used to identify the ship tracks in the first place.

Figure 3.3 shows the distribution of cloud liquid water paths derived using the 3.7- $\mu\text{m}$  channel for ship track (solid black line), control 1 (dotted blue line), and control 2 (dashed red line) pixels. The liquid water path,  $LWP$ , was taken to be given by

$$LWP = \frac{2}{3} R_e \tau_c \rho \quad (3.1)$$

where  $\rho = 1 \text{ g cm}^{-3}$  is the density of water,  $R_e$  is the cloud droplet effective radius, and  $\tau_c$  is the cloud optical depth. Means and standard deviation of the means for the distributions of liquid water paths are given for the ship track and control pixels. The polluted ship track pixels appeared to have less liquid water than the unpolluted

control pixels. The controls had almost equal amounts of liquid water, the difference being attributed to the natural variability in the clouds. One explanation for why the ship track pixels had somewhat less liquid water than the nearby unpolluted control pixels might be due to the entrainment of dry air from above the clouds. The entrained dry air evaporates the smaller cloud droplets in the ship track pixels more readily than the larger droplets in the control pixels (Ackerman et al., 2004).

Figure 3.4 shows similar distributions of droplet effective radii and cloud liquid water paths with the means and standard deviations obtained using the 1.6- $\mu\text{m}$  and the 2.1- $\mu\text{m}$  reflectances. These results, plus those discussed previously, are all summarized in Table 3.1. The means and standard deviation of the means for the ship track and control pixels are given for the cloud visible optical depths, cloud droplet effective radii derived using the 1.6, 2.1, and 3.7- $\mu\text{m}$  channels, and the associated cloud liquid water paths. In this table the means and standard deviations were combined for the control 1 and control 2 pixels. The differences (ship – control) and the root mean square (rms) of the standard deviations of the distributions for the ship track and the control pixels are also given.

Based on the results listed in Table 3.1, the mean cloud optical depths for the ship track pixels were greater than the mean cloud optical depths for the control pixels and this difference was statistically significant. Moreover, the mean droplet radii for the ship track pixels were smaller than in the nearby control pixels by 2.6 – 2.9  $\mu\text{m}$ . The differences were highly significant. Of course, ship track droplet effective radii were smaller because the enhanced reflectivities in the near infrared were used to identify the polluted pixels. Interestingly, the droplet effective radii obtained with the

2.1- $\mu\text{m}$  channel were slightly larger for the control pixels than those obtained with the 1.6 and 3.7- $\mu\text{m}$  derived droplet radii. The differences, however, are within the errors anticipated for such retrievals (Nakajima and King, 1990). In addition, the ship track pixels had less liquid water than did the nearby control pixels based on the results for all the near infrared channels. Ship track pixels had approximately 7 to 11  $\text{gm}^{-2}$  less liquid water than the control pixels. The difference in the cloud liquid water was larger for the droplet effective radii derived using the 2.1- $\mu\text{m}$  channel than for the 1.6- $\mu\text{m}$  channel, and larger still for the droplet effective radii derived using the 3.7- $\mu\text{m}$  channel than for the 2.1- $\mu\text{m}$  channel.

Table 3.2 shows the means and standard error of the means for the differences in cloud optical depths, droplet effective radii, and cloud liquid water paths between the ship track and controls and between both controls. The differences were calculated on a segment-by-segment basis. Calculating the differences on a segment-by-segment basis reduces the variability arising from variations in the mean properties for the segments. The results in Table 3.2 show that for droplet effective radii, cloud optical depths, and cloud liquid water paths, the differences between the ship and the controls were statistically significant. They also show that the differences between both controls were also significant for droplet effective radii and cloud liquid water path. Ideally, the clouds comprising the controls should have been the same. Because of the manner control 1 and control 2 pixels were selected by the automated scheme, natural gradients within the clouds might have led to slight differences in the cloud properties between one control and the other. To verify whether the selection criteria coupled with natural geographic gradients could have caused these differences,

distance-weighted great circle bearings and the distance between controls were calculated.

Figure 3.5 shows the average distance between control 1 and control 2 and the distance-weighted great circle bearings between the controls. The means and standard error of the means for the distributions are also given. The distance weighted-bearings were given by

$$\langle \theta \rangle = \frac{\sum_i d_i \theta_i}{\langle d \rangle} \quad (3.2)$$

where  $d_i$  was the distance between the controls in each segment,  $\theta_i$  was the bearing between the controls, and  $\langle d \rangle$  was the average distance between controls. The mean of the distance-weighted bearings distribution was 110.2 degrees. This shows that control 1 was always oriented to the northwest of control 2. It also shows that going from east-southeast to west-northwest in the Pacific Ocean, there was a natural gradient within the clouds where the droplet effective radii of clouds were slightly smaller near the coast of California. Interestingly, the optical depths were slightly larger nearer the coast. These results are consistent with casual inspection of the near infrared imagery, which suggest that clouds near the coast are often polluted by plumes from the major urban centers of San Francisco and Los Angeles.

Figure 3.6 shows the changes in cloud optical depths, droplet effective radii, and cloud liquid water paths. The distributions represent the mean differences between the ship and controls (solid blue line) and the mean differences between both controls (dashed red line). The means and standard error of the means for these differences are given. Because of the gradients within the clouds going from east-

southeast to west-northwest, the sign of the differences for the controls was randomly selected in creating the distributions that are shown in Figure 3.6 so as to minimize the natural variability within the clouds. These results indicate that the differences between the controls in droplet effective radii, cloud optical depth, and liquid water path were not significantly different than zero. The differences between the ship and the controls, however, were significant. Table 3.3 shows the 99% confidence intervals for droplet effective radii, cloud optical depth, cloud liquid water path, and cloud top altitude. With the exception of cloud top altitude, the averages were significantly different from each other at the 99% confidence level. The confidence interval for cloud top altitude indicated, however, that there was no significant change in cloud altitude. At the 99% confidence level, the average altitudes were not significantly different from each other. The droplet effective radii for the polluted pixels were  $\sim 2.5 - 3.0 \mu\text{m}$  smaller than those of the nearby unpolluted pixels, and the cloud optical depths for the polluted pixels were on average 2.15 larger than the optical depths of the unpolluted pixels. Clearly, the polluted clouds had smaller droplets and they had larger numbers of droplets. In terms of liquid water path, the polluted pixels lost  $\sim 7$  to  $\sim 11 \text{ gm}^{-2}$  of liquid water when compared with the nearby unpolluted clouds. Table 3.4 summarizes these results of the differences.

Figure 3.7 shows two distributions for cloud top height. The first distribution is the average cloud top height for ship track pixels (solid black line), control 1 pixels (dotted blue line), and control 2 pixels (dashed red line). The second distribution is the mean difference between the ship and controls (solid blue line) and the mean difference between both controls (dashed red line). Means and standard deviation of

the means are given in a, and in b the means and standard error the means are given. In both distributions, segments that showed cloud top heights less than 0.4 km were not analyzed. The retrievals for these low-level clouds are unreliable because they are highly sensitive to errors in the properties inferred for the underlying ocean. Therefore, clouds with altitudes below 0.4 km were removed from the analysis. The results in Fig. 3.7 indicate that cloud top height is the same for the ship track and control pixels with an average height of 1.3 km. The results also indicate that the differences between the ship and the controls and differences between both controls in cloud top height did not differ significantly from zero as shown in Table 3.3.

Because they found no significant difference in the optical depths of the polluted and unpolluted clouds, Coakley and Walsh (2002) chose to examine clouds that had the largest response to the underlying ships. They selected cases for which droplet radii changed by more than  $2 \mu\text{m}$ . Following Coakley and Walsh, when changes in the droplet effective radii were greater than or equal to  $2 \mu\text{m}$  the percent difference in cloud properties between the ship track pixels and the control pixels increased significantly for the cloud optical depth and droplet effective radius. Similarly, the cloud liquid water paths suffered larger percentage losses. Table 3.5 shows the results for the different cloud properties when the change in droplet effective radius was greater than or equal to  $2 \mu\text{m}$ . The results are given for the radii derived using each of the near infrared wavelengths. The number of segments that went into the analysis for which the change in droplet effective radii were greater than or equal to  $2 \mu\text{m}$  varied depending on the wavelength. Generally, the number of

segments was 450 – 550 less than when all changes in droplet effective radii were included.

As was the case in the Coakley and Walsh (2002) study, and as indicated in Tables 3.1 and 3.5, the segments that had changes in droplet effective radii greater than or equal to 2  $\mu\text{m}$  corresponded to clouds that had smaller optical depths and larger droplet effective radii. The difference between the ship and the controls in cloud liquid water path ranged from ~5% to ~8%. For clouds with changes in droplet effective radii greater than or equal to 2  $\mu\text{m}$  the difference ranged from ~6% to ~12%. This difference, however, was much smaller than the ~20% difference found by Coakley and Walsh (2002).

Table 3.6 shows the means and standard error of the means for the differences in droplet effective radii, cloud optical depths, and cloud liquid water paths between the ship and controls and between both controls when track segments had a change in droplet radii greater than or equal to 2  $\mu\text{m}$ . The results indicate that the differences between the controls for droplet effective radius, cloud optical depth, and cloud liquid water path were not significantly different than zero. The differences between the ship and controls, on the other hand, were significant. Table 3.7 shows the 99% confidence intervals for the cloud properties when track segments had a change in droplet radii greater than or equal to 2  $\mu\text{m}$ . Not one of the observed confidence intervals contained zeros showing that the means were significantly different from each other at the 99% confidence level. The droplet effective radii for the polluted pixels were ~4.0 to ~6.0  $\mu\text{m}$  smaller than those of the nearby unpolluted pixels, and the cloud optical depths for the polluted pixels were ~2.5 to ~3.5 larger than the optical depths of the

unpolluted pixels. The polluted clouds lost  $\sim 7$  to  $\sim 18.5 \text{ gm}^{-2}$  of liquid water compared to the nearby unpolluted clouds.

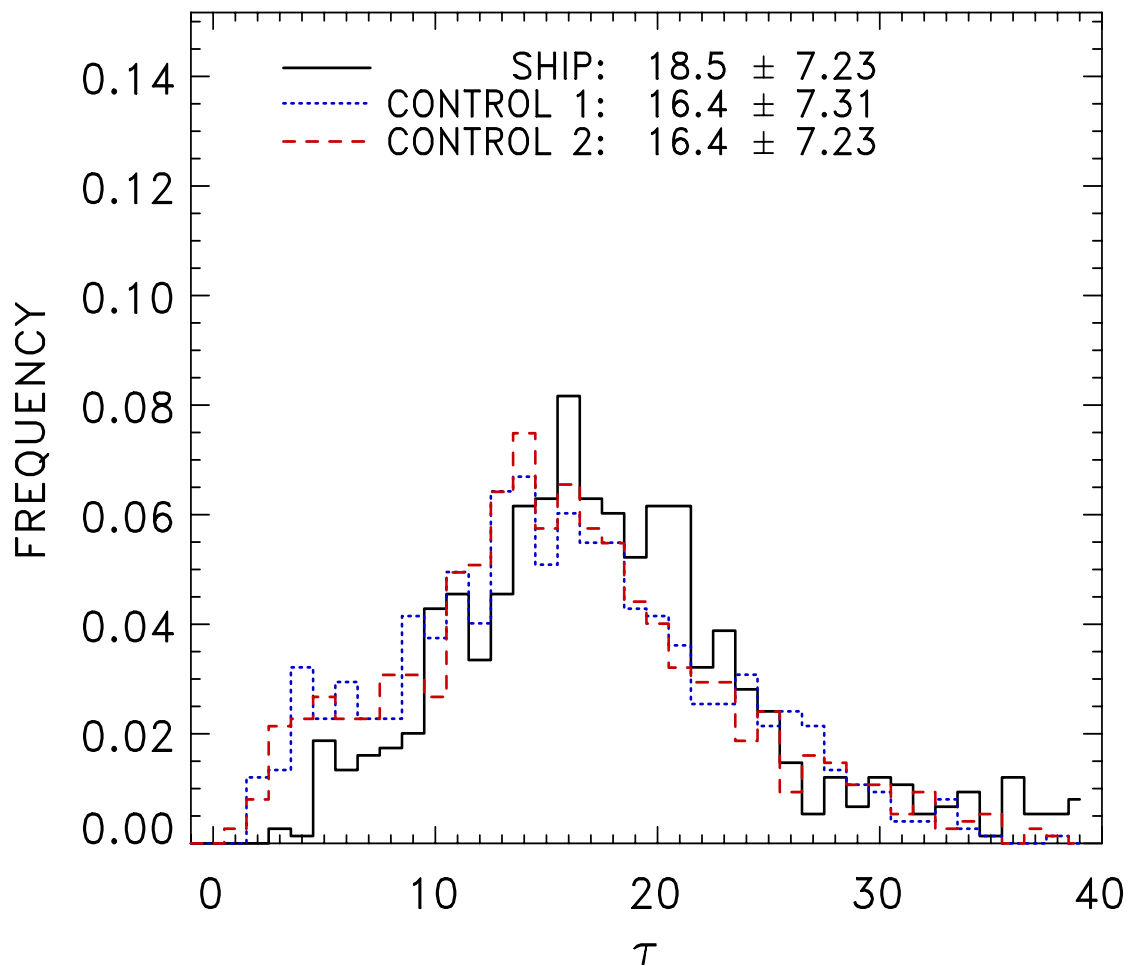


FIGURE 3.1. Cloud optical depths for the ship track pixels (solid black line), control 1 pixels (dotted blue line), and the control 2 pixels (dashed red line) taken from 20-pixel track segments. Means and standard deviation of the means for the distributions are given.

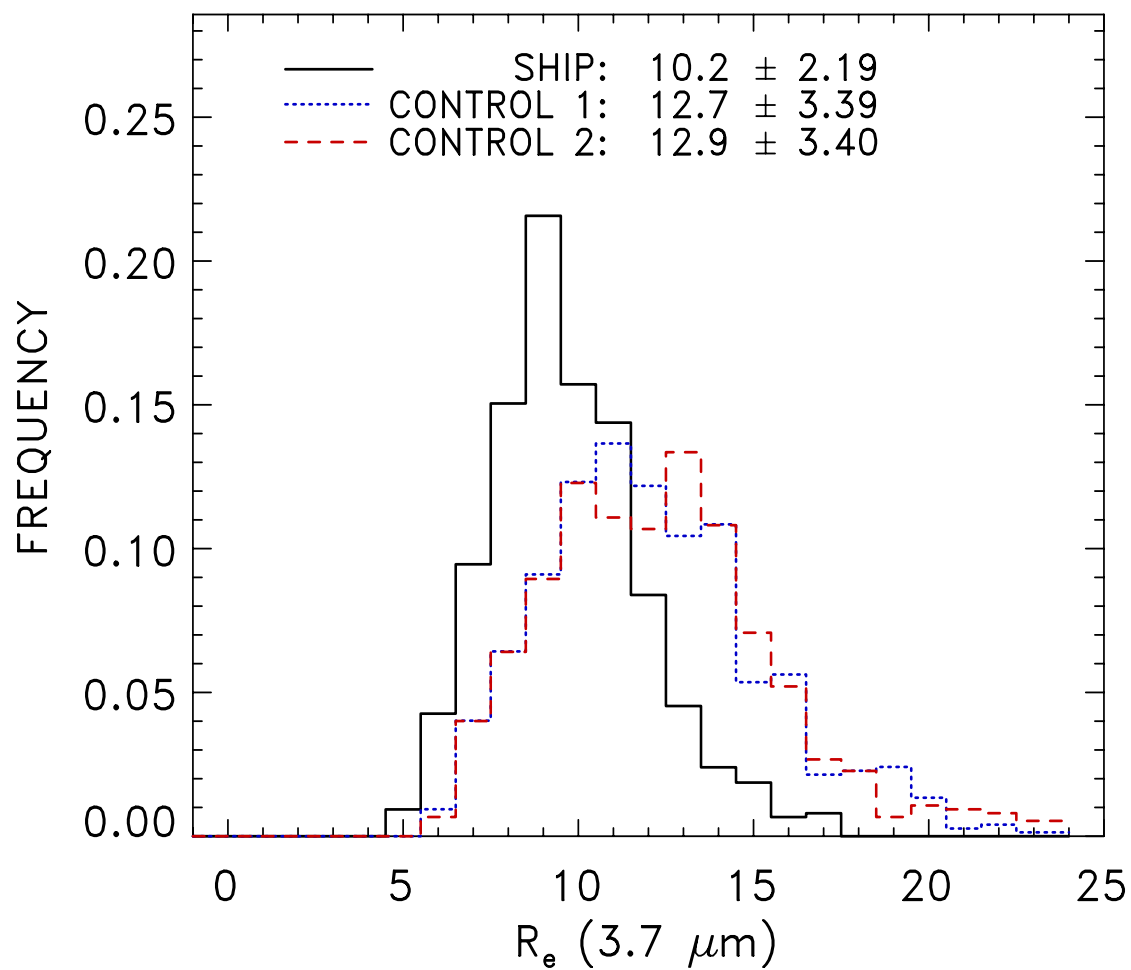


FIGURE 3.2. Same as figure 3.1 except for droplet effective radius derived using the 3.7- $\mu\text{m}$  channel.

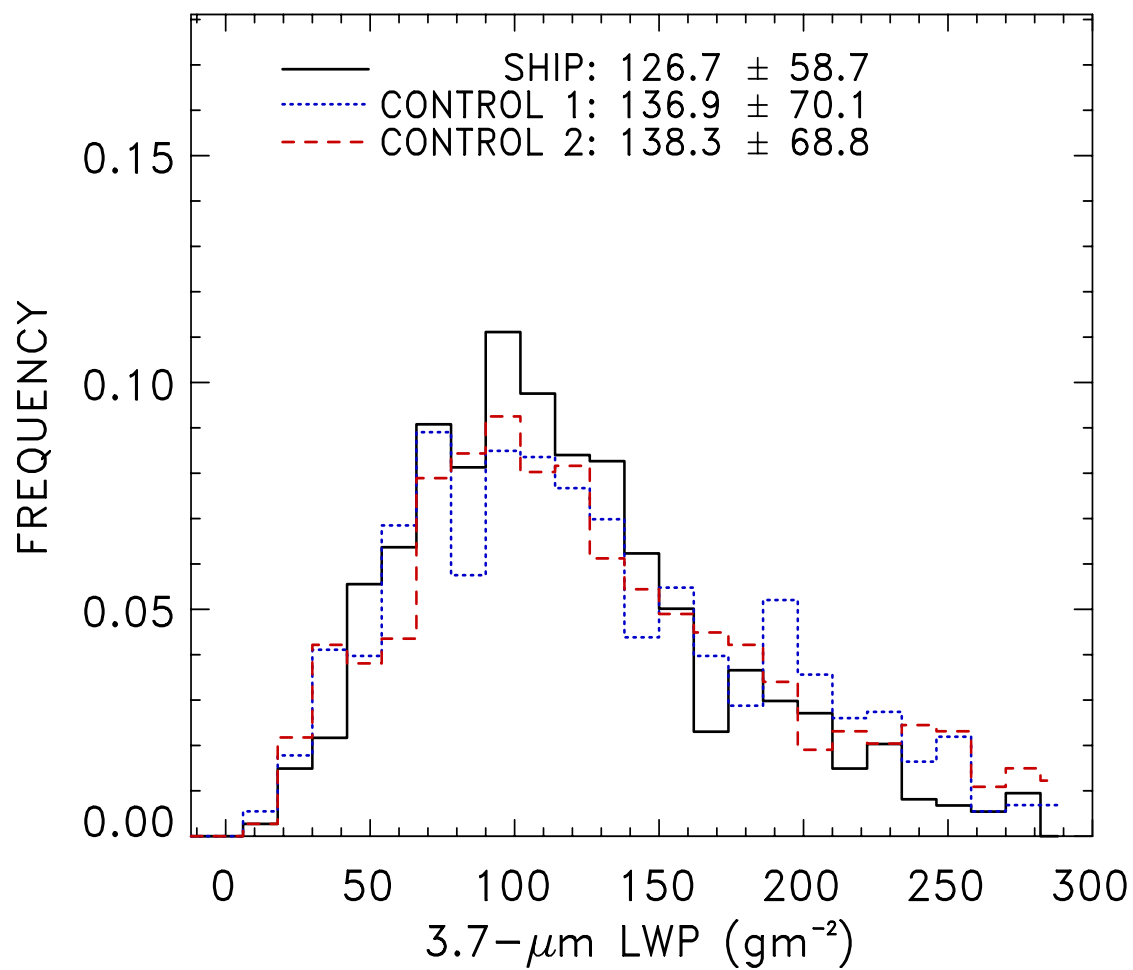


FIGURE 3.3. Same as figure 3.1 except for liquid water path derived using the 3.7- $\mu\text{m}$  channel.

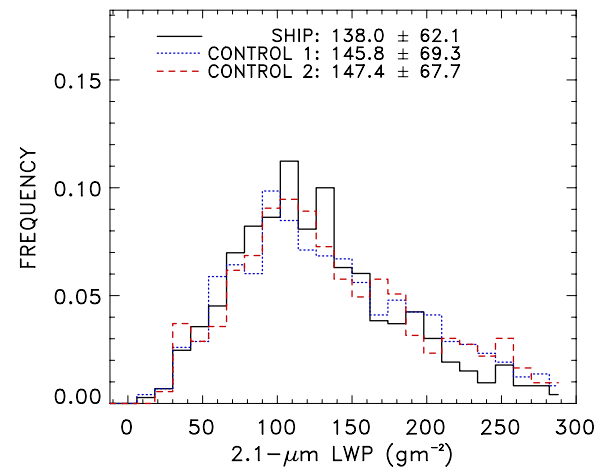
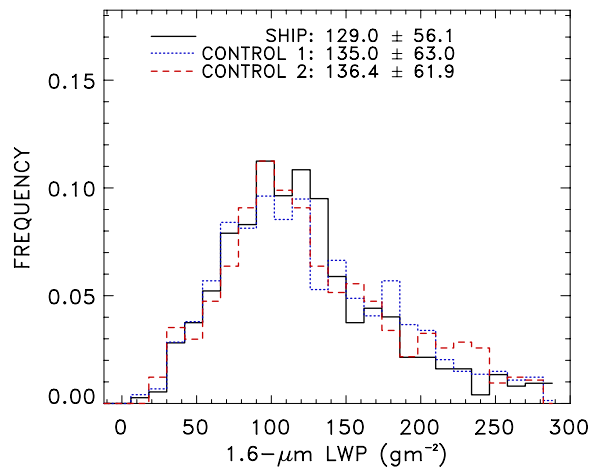
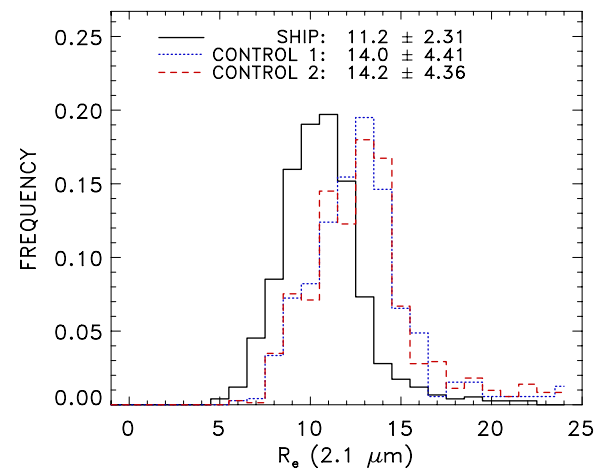
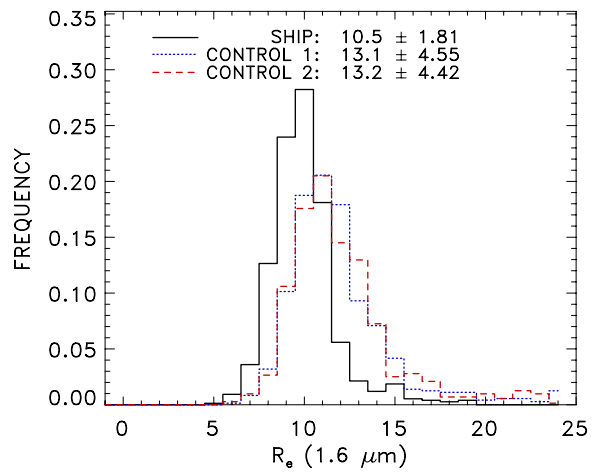


FIGURE 3.4. Same as figure 3.1 except for droplet effective radii and cloud liquid water paths derived using the 1.6 and 2.1- $\mu\text{m}$  channels.

TABLE 3.1. Means and standard deviation of the means for cloud optical depths, cloud droplet effective radii derived using the 1.6, 2.1, and 3.7- $\mu\text{m}$  channels, and the associated cloud liquid water paths for the ship track and controls. The difference between the ship and the controls and the rms of the standard deviation of the means is also shown for each of the cloud properties. N = number of track segments over which cloud properties were averaged.

N=751	$R_e$ ( $\mu\text{m}$ )			$\tau$	LWP ( $\text{gm}^{-2}$ )		
	1.6	2.1	3.7		1.6	2.1	3.7
Ship	$10.5 \pm 1.81$	$11.2 \pm 2.31$	$10.2 \pm 2.19$	$18.5 \pm 7.23$	$129.0 \pm 56.1$	$138.0 \pm 62.1$	$126.7 \pm 58.7$
Controls	$13.2 \pm 4.49$	$14.1 \pm 4.34$	$12.8 \pm 3.40$	$16.4 \pm 7.27$	$135.6 \pm 62.5$	$146.6 \pm 68.5$	$137.6 \pm 69.5$
Difference	$-2.7 \pm 3.42$	$-2.9 \pm 3.48$	$-2.6 \pm 2.86$	$2.1 \pm 7.25$	$-6.60 \pm 59.4$	$-8.61 \pm 65.4$	$-10.9 \pm 64.3$

TABLE 3.2. Means and standard error of the means for the differences between ship and controls and the differences between control 1 and control 2 for cloud optical depths, cloud droplet effective radii derived using the 1.6, 2.1, and 3.7- $\mu\text{m}$  channels, and the associated cloud liquid water paths. N = number of track segments over which cloud properties were averaged.

N=751	$R_e$ ( $\mu\text{m}$ )			$\tau$	LWP ( $\text{gm}^{-2}$ )		
	1.6	2.1	3.7		1.6	2.1	3.7
Ship – Controls	$-2.70 \pm 0.11$	$-2.90 \pm 0.10$	$-2.58 \pm 0.07$	$2.14 \pm 0.12$	$-6.60 \pm 0.89$	$-8.60 \pm 1.02$	$-10.90 \pm 1.12$
Control 1 – Control 2	$0.16 \pm 0.10$	$0.18 \pm 0.08$	$-0.15 \pm 0.07$	$0.02 \pm 0.14$	$1.50 \pm 1.40$	$1.75 \pm 1.52$	$1.55 \pm 1.55$

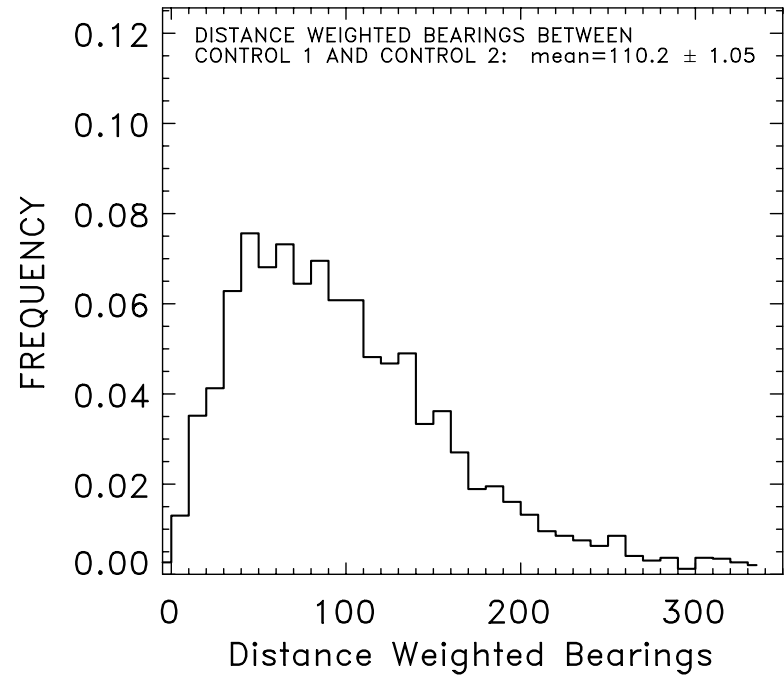
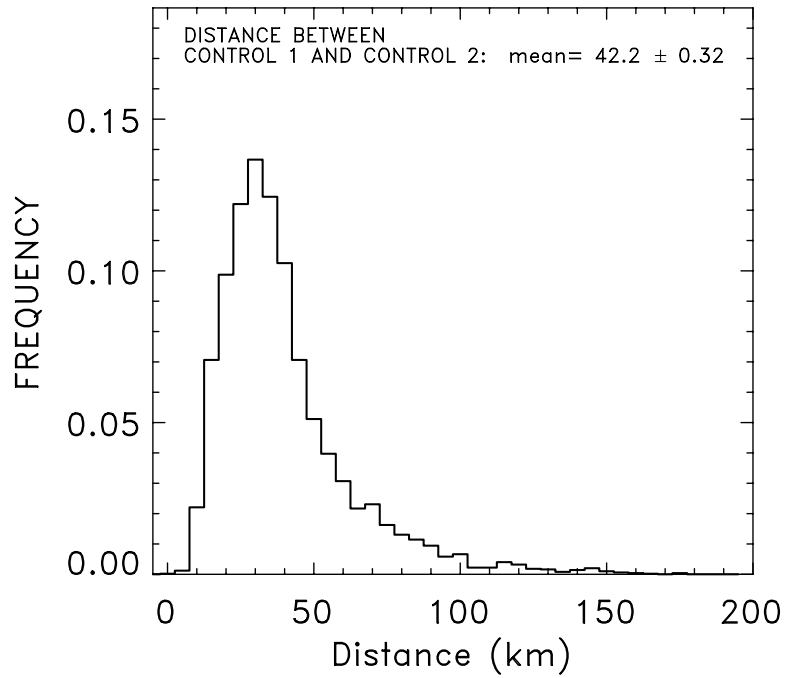


FIGURE 3.5. Average distance and the distance-weighted bearings. Means and standard error of the means are shown.

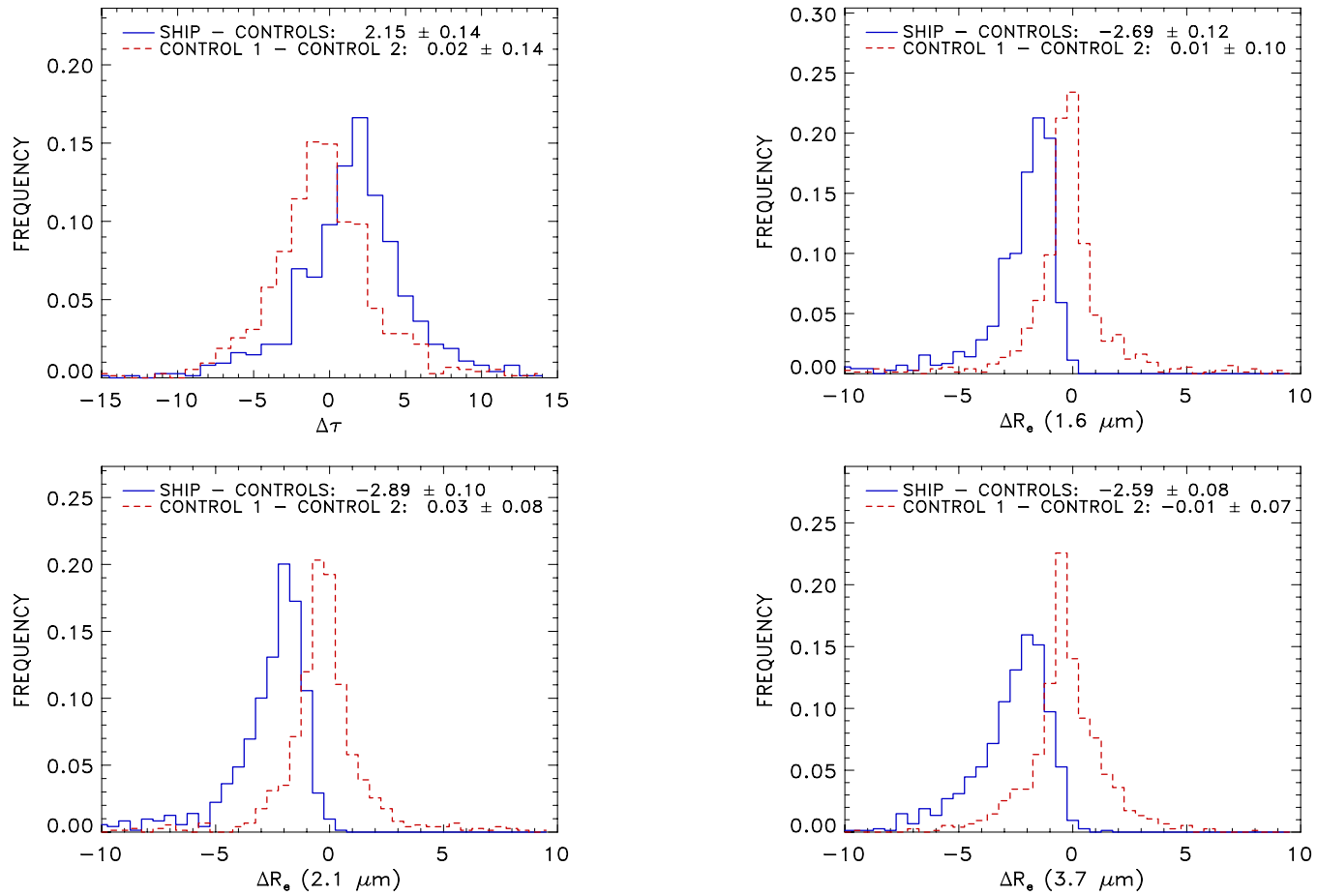


FIGURE 3.6. Mean differences between the ship and controls (solid blue line) and between control 1 and control 2 (dashed red line) for cloud optical depth, droplet effective radii derived using the 1.6, 2.1 and 3.7- $\mu\text{m}$  channels, and the associated cloud liquid water paths, taken from 20-pixel track segments. The means and standard error of the means are given.

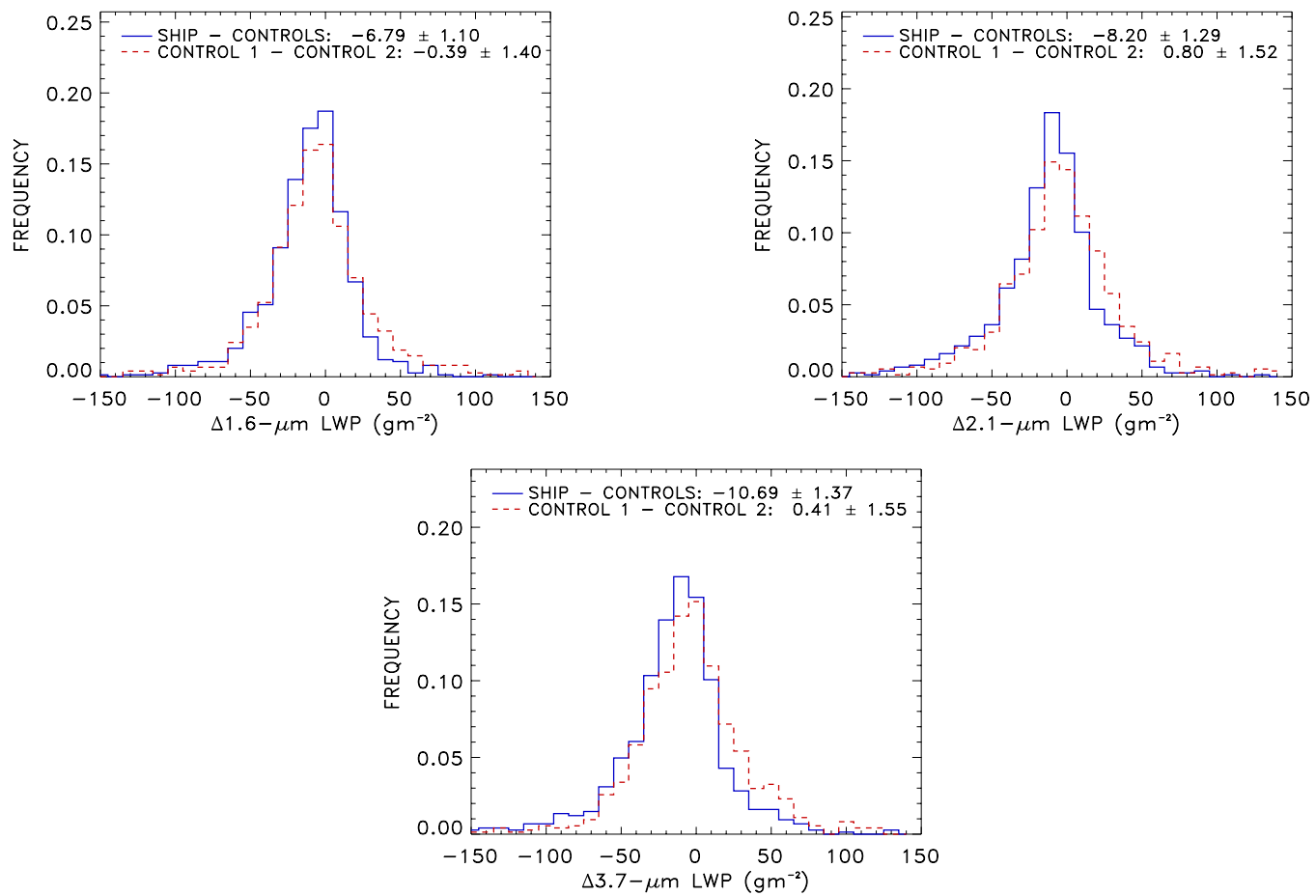


Figure 3.6. (Continued)

TABLE 3.3. Means for the differences between ship and controls along with the 99% confidence intervals for each of the cloud properties. N = number of track segments over which cloud properties were averaged.

N=751	$R_e$ ( $\mu\text{m}$ )			$\tau$	LWP ( $\text{gm}^{-2}$ )			$z_c$ (km)
	1.6	2.1	3.7		1.6	2.1	3.7	
Confidence Interval	$-2.69 \pm 0.23$	$-2.89 \pm 0.24$	$-2.59 \pm 0.22$	$2.15 \pm 0.35$	$-6.79 \pm 1.01$	$-8.20 \pm 1.06$	$-10.69 \pm 1.05$	$-0.01 \pm 0.09$

TABLE 3.4. Means and standard error of the means for the differences between ship and controls and the randomized differences between control 1 and control 2 for cloud optical depth, cloud droplet effective radius derived using the 1.6, 2.1, and 3.7- $\mu\text{m}$  channels, and the associated cloud liquid water paths. N = number of track segments over which cloud properties were averaged.

N=751	$R_e$ ( $\mu\text{m}$ )			$\tau$	LWP ( $\text{gm}^{-2}$ )		
	1.6	2.1	3.7		1.6	2.1	3.7
Ship – Controls	$-2.69 \pm 0.12$	$-2.89 \pm 0.10$	$-2.59 \pm 0.08$	$2.15 \pm 0.14$	$-6.79 \pm 1.10$	$-8.20 \pm 1.29$	$-10.69 \pm 1.37$
Control 1 – Control 2	$0.01 \pm 0.10$	$0.03 \pm 0.08$	$-0.01 \pm 0.07$	$0.03 \pm 0.14$	$-0.39 \pm 1.40$	$0.80 \pm 1.52$	$0.41 \pm 1.55$

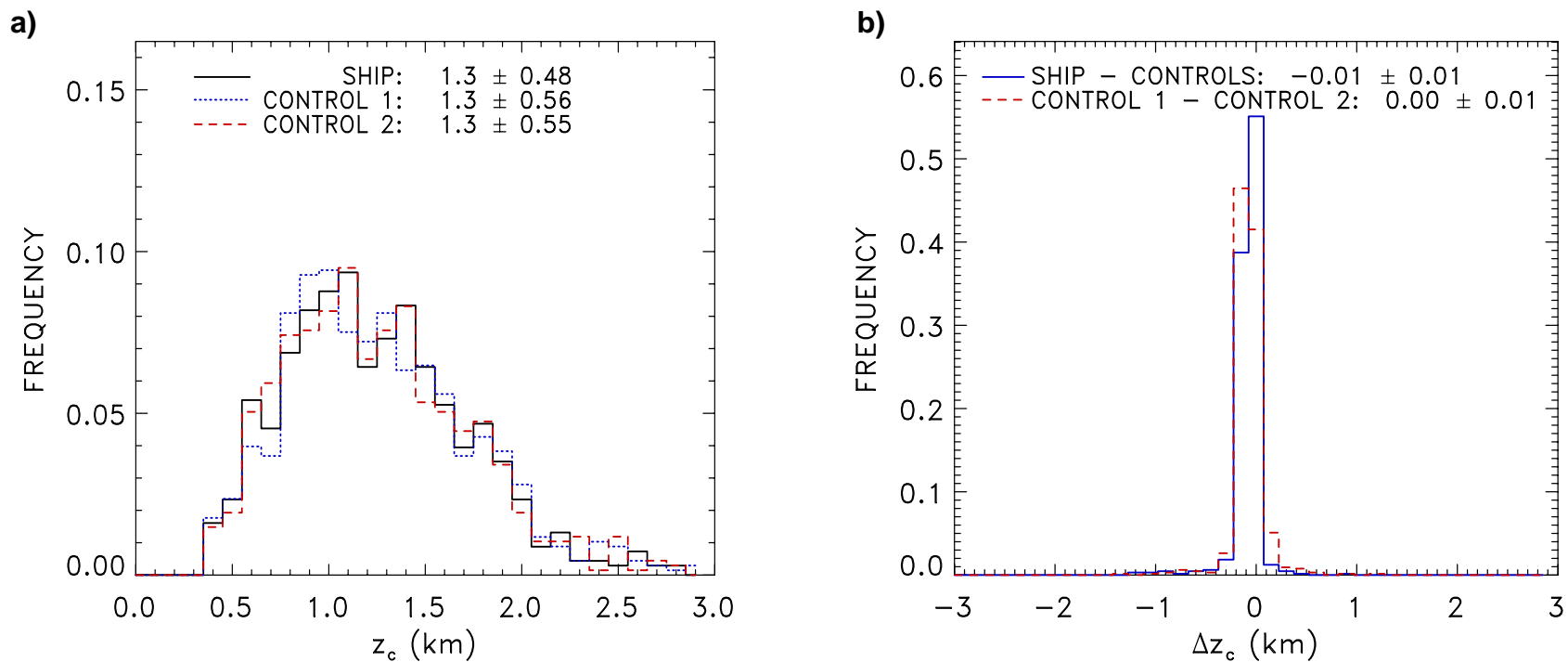


FIGURE 3.7. Distribution a) shows the average cloud top height for the ship track pixels (solid black line), control 1 pixels (dotted blue line), and the control 2 pixels (dashed red line) taken from 20-pixel track segments. Distribution b) shows the mean differences between the ship and controls (solid blue line) and the mean differences between both controls (dashed red line). Means and standard deviation of the means are given in a) and means and standard error of the means are given in b).

TABLE 3.5. Same as Table 3.1 except segments were kept only if they had changes in cloud droplet effective radii that were greater than or equal to  $2 \mu\text{m}$ .

$\Delta R_e \geq 2 \mu\text{m}$			
N=211	1.6 $\mu\text{m}$		
	$R_e (\mu\text{m})$	$\tau$	LWP ( $\text{gm}^{-2}$ )
Ship	$11.5 \pm 2.42$	$16.2 \pm 7.86$	$121.9 \pm 59.2$
Controls	$17.4 \pm 6.01$	$12.6 \pm 7.39$	$129.1 \pm 66.7$
Difference	$-5.9 \pm 4.58$	$3.6 \pm 7.63$	$-7.2 \pm 63.1$
N=277	2.1 $\mu\text{m}$		
	$R_e (\mu\text{m})$	$\tau$	LWP ( $\text{gm}^{-2}$ )
Ship	$11.8 \pm 2.69$	$15.4 \pm 7.46$	$134.2 \pm 64.9$
Controls	$16.9 \pm 5.34$	$12.0 \pm 7.06$	$142.7 \pm 69.1$
Difference	$-5.1 \pm 4.23$	$3.4 \pm 7.26$	$-8.50 \pm 67.0$
N=287	3.7 $\mu\text{m}$		
	$R_e (\mu\text{m})$	$\tau$	LWP ( $\text{gm}^{-2}$ )
Ship	$10.8 \pm 2.15$	$15.4 \pm 7.38$	$131.2 \pm 60.1$
Controls	$15.1 \pm 3.37$	$12.1 \pm 7.03$	$149.5 \pm 75.1$
Difference	$-4.3 \pm 2.83$	$3.3 \pm 7.21$	$-18.3 \pm 68.0$

TABLE 3.6. Means and standard error of the means for differences between ship and controls and randomized differences between control 1 and control 2 for droplet effective radii derived using the 1.6, 2.1 and 3.7- $\mu\text{m}$  channels, cloud optical depths, and cloud liquid water paths. Differences were taken on a segment-by-segment basis. N = the number of track segments over which the cloud properties were averaged.

$\Delta R_e \geq 2 \mu\text{m}$			
N=211	1.6 $\mu\text{m}$		
	$\Delta R_e (\mu\text{m})$	$\Delta\tau$	$\Delta\text{LWP} (\text{gm}^{-2})$
Ship – Controls	$-5.84 \pm 0.33$	$3.66 \pm 0.29$	$-7.22 \pm 2.48$
Control 1 – Control 2	$-0.12 \pm 0.28$	$0.00 \pm 0.24$	$-0.08 \pm 2.88$
N=277	2.1 $\mu\text{m}$		
	$\Delta R_e (\mu\text{m})$	$\Delta\tau$	$\Delta\text{LWP} (\text{gm}^{-2})$
Ship – Controls	$-5.00 \pm 0.22$	$3.33 \pm 0.25$	$-8.67 \pm 2.24$
Control 1 – Control 2	$0.08 \pm 0.18$	$0.09 \pm 0.11$	$-0.53 \pm 2.41$
N=287	3.7 $\mu\text{m}$		
	$\Delta R_e (\mu\text{m})$	$\Delta\tau$	$\Delta\text{LWP} (\text{gm}^{-2})$
Ship – Controls	$-4.17 \pm 0.13$	$2.69 \pm 0.25$	$-18.65 \pm 2.43$
Control 1 – Control 2	$0.06 \pm 0.12$	$0.00 \pm 0.21$	$-0.69 \pm 2.53$

TABLE 3.7. Same as Table 3.3 except segments were kept only if they had changes in cloud droplet effective radii that were greater than or equal to  $2 \mu\text{m}$ .

$\Delta R_e \geq 2 \mu\text{m}$			
N=211	1.6 $\mu\text{m}$		
	$R_e (\mu\text{m})$	$\tau$	LWP ( $\text{gm}^{-2}$ )
Confidence Interval	$-5.84 \pm 0.45$	$3.66 \pm 0.69$	$-7.22 \pm 1.94$
N=277	2.1 $\mu\text{m}$		
	$R_e (\mu\text{m})$	$\tau$	LWP ( $\text{gm}^{-2}$ )
Confidence Interval	$-5.00 \pm 0.40$	$3.16 \pm 0.59$	$-8.67 \pm 1.76$
N=287	3.7 $\mu\text{m}$		
	$R_e (\mu\text{m})$	$\tau$	LWP ( $\text{gm}^{-2}$ )
Confidence Interval	$-4.17 \pm 0.33$	$2.69 \pm 0.57$	$-18.65 \pm 1.69$

### 3.2 *Aqua* Observations

For the *Aqua* overpasses, there were 694 track segments that yielded comparisons between polluted and unpolluted clouds for the summer months June – August, 2002, and May – August, 2003 – 2004. Figure 3.8 shows the distribution of optical depths for the polluted ship track pixels (solid black line) and for the pixels identified as unpolluted control 1 (dotted blue line) pixels on one side of the track and control 2 (dashed red line) pixels on the other side. Means and standard deviation of the means for the distributions of the optical depths for the ship and both controls are given. The distributions were acquired for 20-pixel segments measured along the track and total domain size on either side of the track that equaled the width of the ship track and the two controls on either side. The widths of the controls were set to be approximately equal to the width of the track. The means and standard deviations for the controls were essentially identical, indicating that the clouds on either side of the track were the same. The variation between control 1 and control 2 pixels resulted from the natural variability of the clouds. On the other hand, the optical depths for the ship track pixels were significantly larger than those for the control pixels. The polluted clouds had larger reflectivities than the nearby unpolluted clouds.

Figure 3.9 shows the distribution of droplet effective radii derived using the 3.7- $\mu\text{m}$  channel for ship track pixels (solid black line), control 1 pixels (dotted blue line), and control 2 pixels (dashed red line). Again, the means and standard deviation of the means for the distributions are given. The results in Fig. 3.9 indicate that the difference in the 3.7- $\mu\text{m}$  droplet effective radii between control 1 and control 2 pixels were nonexistent. Moreover, there was a significant difference in the cloud droplet

radii for the ship track and the nearby control pixels. The ship track pixels had droplet effective radii  $2.4\ \mu\text{m}$  smaller than those of the nearby controls. The smaller droplets were caused by the higher concentration of cloud condensation nuclei in the ship's exhaust plume. The clouds on either side of the track were within the uncertainty associated with the natural variability of the clouds.

Figure 3.10 shows the distribution of cloud liquid water paths derived using the  $3.7\text{-}\mu\text{m}$  channel to determine droplet effective radii for ship track pixels (solid black line), control 1 pixels (dotted blue line), and control 2 pixels (dashed red line). Means and standard deviation of the means for the distributions of liquid water paths are given for the ship track and control pixels. The polluted ship track pixels appeared to have less liquid water than the unpolluted control pixels. There was virtually no difference in liquid water between the controls with the difference being attributed to the natural variability in the clouds. Figure 3.11 shows similar distributions of droplet effective radii and cloud liquid water paths with the mean and standard deviations obtained using the  $1.6$  and  $2.1\text{-}\mu\text{m}$  reflectances to retrieve the droplet radii. These results, plus those discussed previously, are summarized in Table 3.8. The means and standard deviation of the means for the ship track pixels are given for the cloud visible optical depths, cloud droplet effective radii derived using the  $1.6$ ,  $2.1$ , and  $3.7\text{-}\mu\text{m}$  channels, and the associated cloud liquid water paths. The means and standard deviations were combined for the control 1 and control 2 pixels. The differences and the rms of the standard deviations for the distributions between the ship track and the control pixels are also given.

Based on the results listed in Table 3.8, the droplet effective radii derived using the 1.6 and 2.1- $\mu\text{m}$  channels for ship track pixels were significantly smaller than the control pixels, consistent with the results derived using the 3.7- $\mu\text{m}$  channel. The 2.1- $\mu\text{m}$  channel, however, produced droplet effective radii that were slightly larger than those derived using the 1.6 and 3.7- $\mu\text{m}$  channels, but the differences were within the errors anticipated for such retrievals (Nakajima and King, 1990). The mean droplet radii for the ship track pixels were smaller than in the controls by  $\sim 2.6 \mu\text{m}$ . Additionally, the smaller cloud droplets in the ship track pixels coincided with the larger cloud optical depths and the differences in cloud optical depth between the ship track and the control pixels was significant. Furthermore, based on the results for all the near infrared channels, there was less liquid water in the ship track pixels than in the nearby control pixels. Even though the differences were not large, ship track pixels had approximately  $3 - 6 \text{ gm}^{-2}$  less liquid water than the control pixels. Similar to the *Terra* data, the difference in the liquid water was larger for the droplet effective radii derived using the 2.1- $\mu\text{m}$  channel than for the 1.6- $\mu\text{m}$  channel, and larger still for the droplet radii derived using the 3.7- $\mu\text{m}$  channel than for the 2.1- $\mu\text{m}$  channel.

While changes in droplet effective radii were the same for all wavelengths, the larger losses in cloud liquid water for the 3.7- $\mu\text{m}$  channel suggested that smaller changes in cloud optical depth occurred for a given change in droplet effective radii. At the other wavelengths larger changes in cloud optical depth must have occurred for a given change in droplet effective radius. As the shorter wavelength channels see “deeper” into the clouds (Platnick et al. 2000), the dependence of the changes in cloud liquid water on wavelength suggests that not only were droplet sizes changed by the

pollution but that the vertical distribution of droplet size within the cloud was also affected.

Table 3.9 shows the means and standard error of the means for the differences in cloud optical depth, droplet effective radii, and cloud liquid water paths between the ship and controls and between both controls. The differences were calculated on a segment-by-segment basis. The ensemble of differences was constructed to determine whether natural variations in cloud properties gave rise to significant differences in the controls on either side of the track. For the droplet effective radii, cloud optical depths, and cloud liquid water paths the results in Table 3.9 show that the differences between the ship and controls were significant. The results also show that the differences between both controls were significant. Ideally, there should have been no significant differences between the controls. But, as with the *Terra* data, because of the manner in which control 1 and control 2 pixels were chosen any geographic gradient in the clouds would be detected. Figure 3.12 shows the average distance between control 1 and control 2 along with the distance-weighted great circle bearings as calculated by (3.2). The mean of the distance-weighted bearings distribution was 115.6 degrees. This shows that the two controls were chosen so that in going from one to the other meant going from east-southeast to west-northwest. Because there was a natural gradient within the clouds where the droplet effective radii of clouds were slightly smaller near the coast of California, there was a small but significant difference in the droplet effective radii for the two controls.

Figure 3.13 shows the changes in cloud optical depths, droplet effective radii, and cloud liquid water paths. The distributions represent the mean differences

between the ship and controls (solid blue line), and the mean differences between both controls (dashed red line). The means and standard error of the means for these differences are given. Due to the gradients within the clouds going from east-southeast to west-northwest the sign of the differences for the controls was randomly selected when creating the distributions that are shown in Figure 3.13. These results indicate that the differences between control 1 and control 2 in droplet effective radii, cloud optical depth, and liquid water path were not significantly different from zero. The differences between polluted clouds and unpolluted clouds, however, were significant. Table 3.10 shows the 99% confidence intervals for droplet effective radii, cloud optical depth, cloud liquid water paths, and cloud top altitude. With the exception of cloud top altitude, the averages were significantly different from each other at the 99% confidence level. The confidence interval for cloud top altitude indicated, however, that there was no significant change in cloud altitude. At the 99% confidence level, the average altitudes were not significantly different from each other. The polluted clouds had droplet effective radii that were  $\sim 2.5 \mu\text{m}$  smaller than those for the nearby unpolluted clouds. Also, cloud optical depths for the polluted clouds were on average 2.3 larger than optical depths for the unpolluted clouds. Finally, the liquid water paths for the polluted clouds lost  $\sim 3.0$  to  $\sim 5.5 \text{ gm}^{-2}$  of liquid water when compared with the nearby unpolluted clouds. Table 3.11 summarizes these results.

Figure 3.14 shows two distributions for cloud top height. The first distribution shows the average cloud top height for ship track pixels (solid black line), control 1 pixels (dotted blue line), and control 2 pixels (dashed red line). The second distribution shows the mean differences between the ship and controls (solid blue line)

and the mean differences between both controls (dashed red line). Means and standard error deviation of the means are given in a, and in b the means and standard error of the means are given. In both distributions, segments that showed cloud top heights less than 0.4 km were not analyzed. The retrievals for these low-level clouds are unreliable as they are highly sensitive to errors in the properties inferred for the underlying ocean. Clouds with altitudes below 0.4 km were therefore removed from the analysis. The results in Fig. 3.14 indicate that cloud top height is identical for the ship track and control pixels with an average height of 1.1 km. The results also indicate that the differences between the ship and the controls and differences between both controls with respect to cloud top height were not significantly different than zero as shown in Table 3.10.

Table 3.12 shows the results for the droplet effective radii, cloud optical depths, and cloud liquid water paths where the difference in droplet effective radius was greater than or equal to 2  $\mu\text{m}$ . The results are given for the radii derived using each of the near infrared wavelengths. The number of segments that went into the analysis varied depending on wavelength. Generally, though, the number of segments was about 450 segments less than those that had produced successful comparisons when all changes in droplet effective radii were included. As occurred with Coakley and Walsh (2002), when changes in the droplet effective radii were greater than or equal to 2  $\mu\text{m}$ , the percent difference in cloud properties between the ship track pixels and the control pixels increased significantly for cloud optical depths and droplet effective radii. Likewise, cloud liquid water suffered larger percentage losses. The difference in cloud liquid water between the ship and controls ranged from ~4% to 9%

when a change in droplet effective radii greater than or equal to  $2\ \mu\text{m}$  was implemented, up from  $\sim 2.5\%$  to  $\sim 5\%$  when all changes in droplet effective radii were included. Nonetheless, the losses in cloud liquid water were much smaller than the  $\sim 20\%$  loss found by Coakley and Walsh (2002). Furthermore, as in the Coakley and Walsh study and indicated by the results in Tables 3.8 and 3.12, the segments with droplet effective radii greater than or equal to  $2\ \mu\text{m}$  corresponded to clouds that had smaller optical depths and larger droplet effective radii.

Table 3.13 shows the means and standard error of the means for the differences in droplet effective radii, cloud optical depths, and cloud liquid water paths between the ship and controls and between both controls when track segments had a change in droplet radii greater than or equal to  $2\ \mu\text{m}$ . The results indicate that the differences between the controls in droplet effective radii, cloud optical depths, and cloud liquid water paths, when segments had a change in droplet radii greater than or equal to  $2\ \mu\text{m}$ , were not significantly different than zero. The differences between the ship and controls, on the other hand, were significant. Table 3.14 shows the 99% confidence intervals for the cloud properties when track segments had a change in droplet radii greater than or equal to  $2\ \mu\text{m}$ . None of the observed confidence intervals contained zeros showing that the means were significantly different from each other at the 99% confidence level. The droplet effective radii for the polluted pixels were  $\sim 4.0$  to  $\sim 5.0\ \mu\text{m}$  smaller than those of the nearby unpolluted pixels, and the cloud optical depths for the polluted pixels were  $\sim 3$  larger than the optical depths of the unpolluted pixels. In terms of liquid water path, the polluted clouds lost  $\sim 5$  to  $\sim 11\ \text{gm}^{-2}$  liquid water compared to the nearby unpolluted clouds.

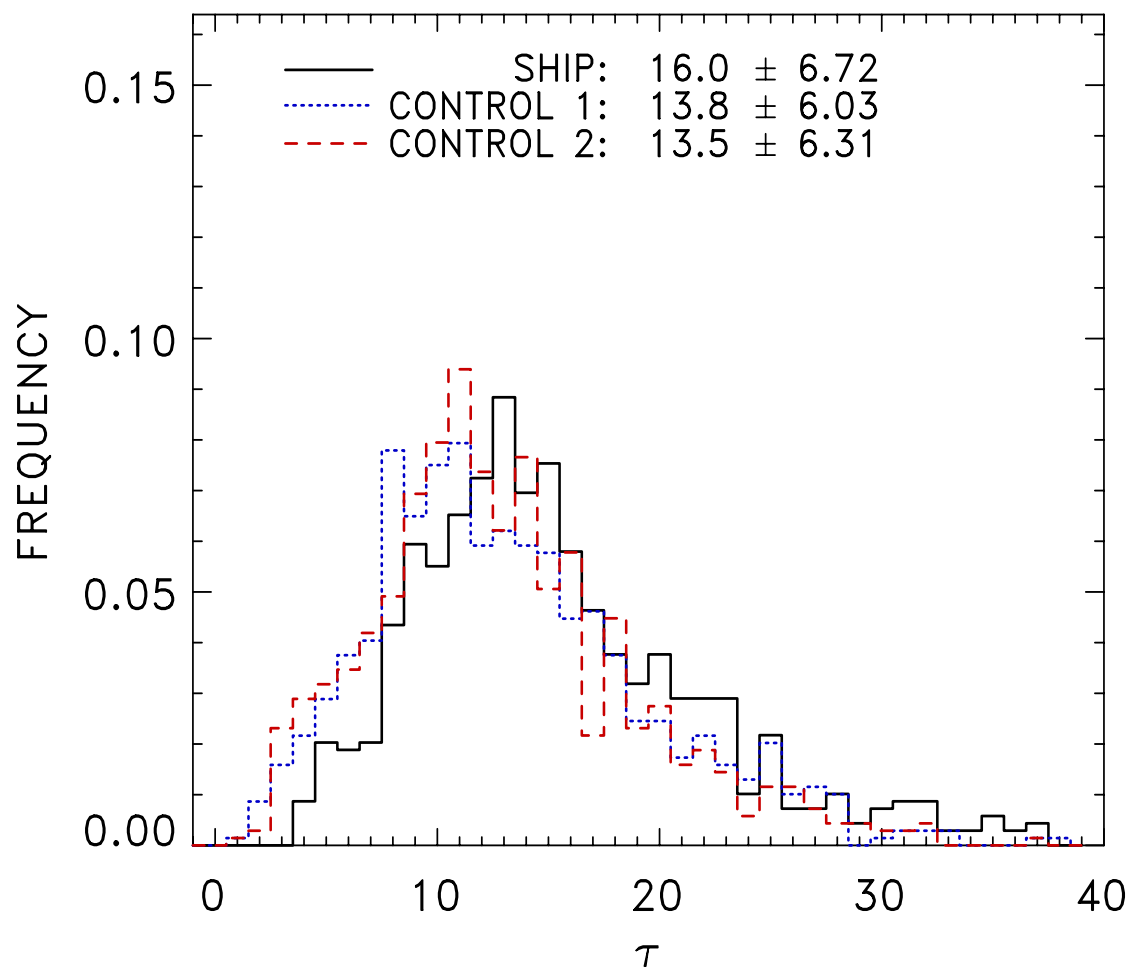


FIGURE 3.8. Cloud optical depths for the ship track pixels (solid black line), control 1 pixels (dotted blue line), and the control 2 pixels (dashed red line) taken from 20-pixel track segments. The means and standard deviation of the means for the distributions are given.

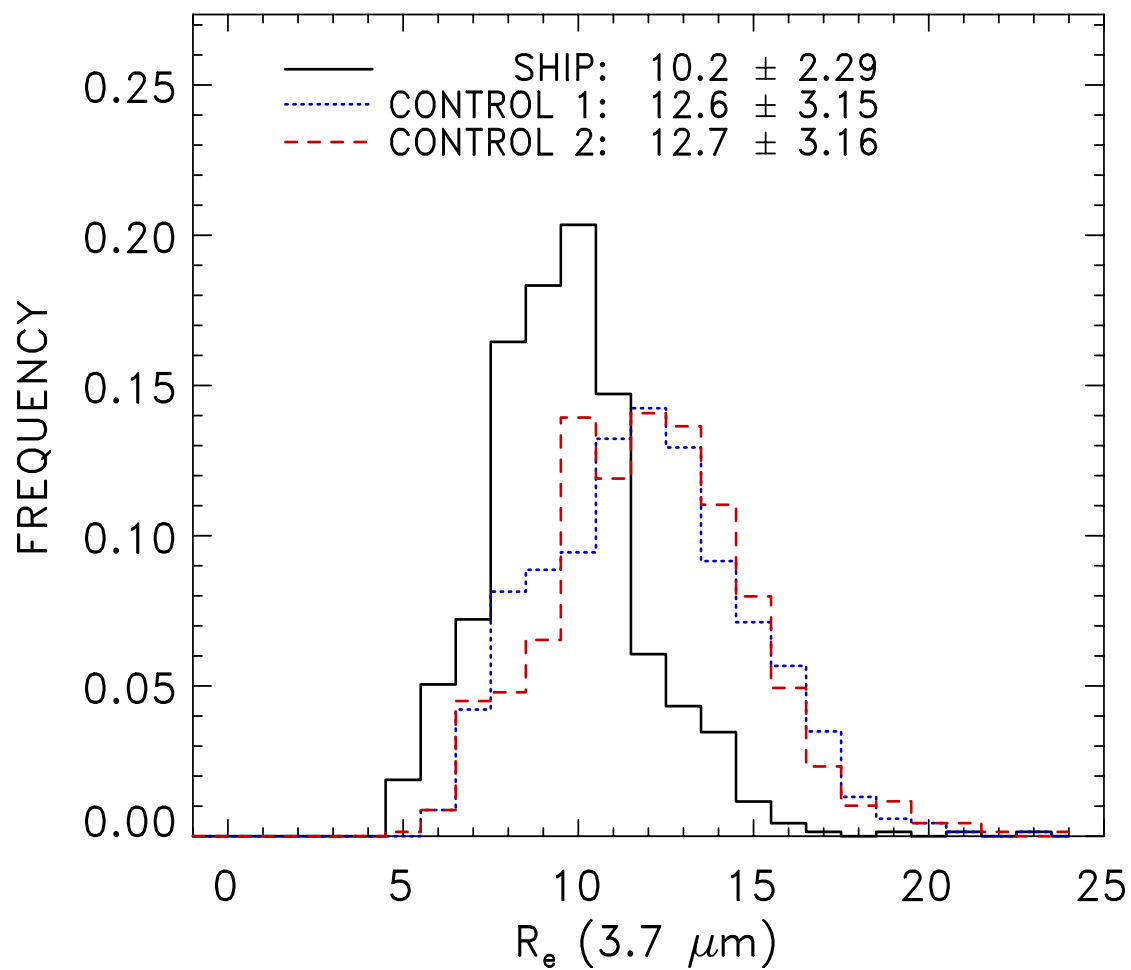


FIGURE 3.9. Same as figure 3.8 except for droplet effective radii derived using the 3.7- $\mu\text{m}$  channel.

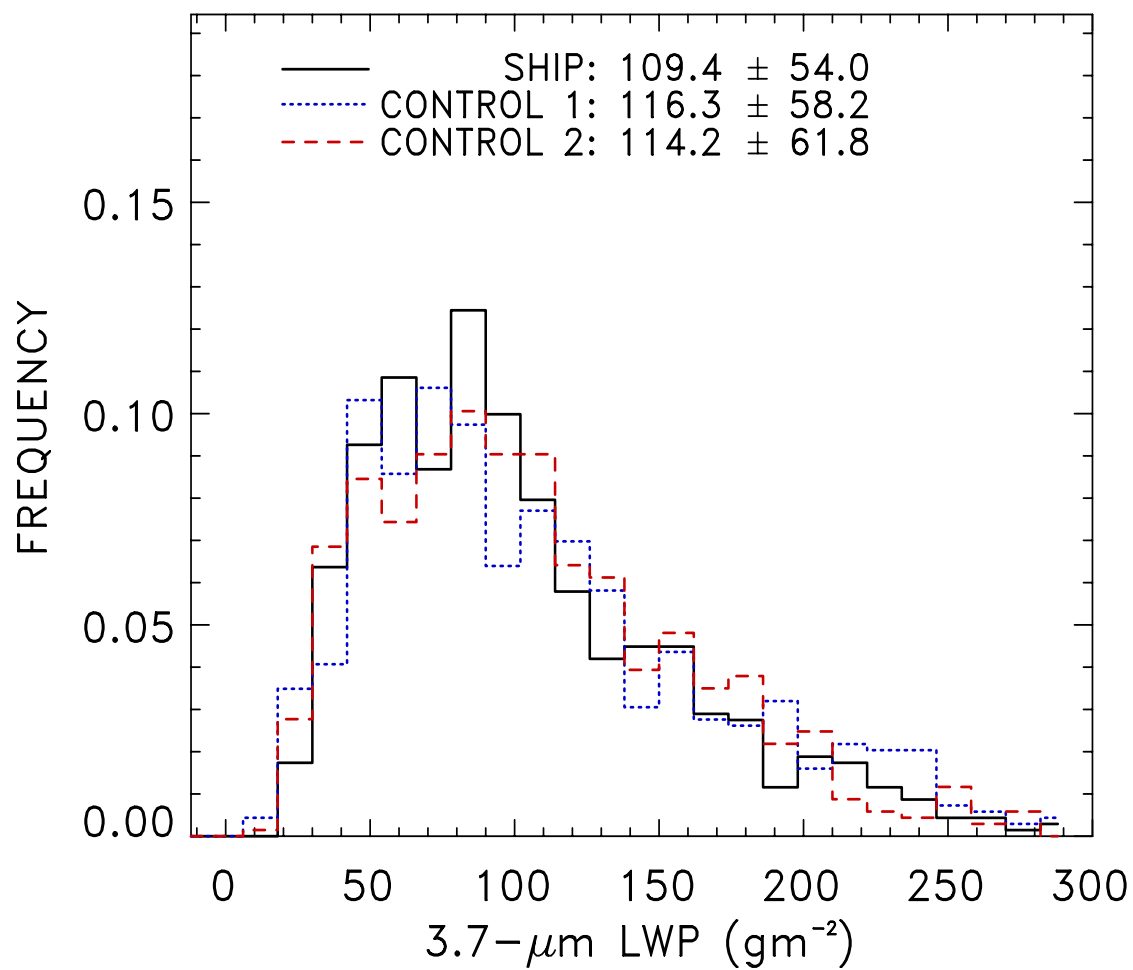


FIGURE 3.10. Same as figure 3.8 except for liquid water path derived using the 3.7-μm channel.

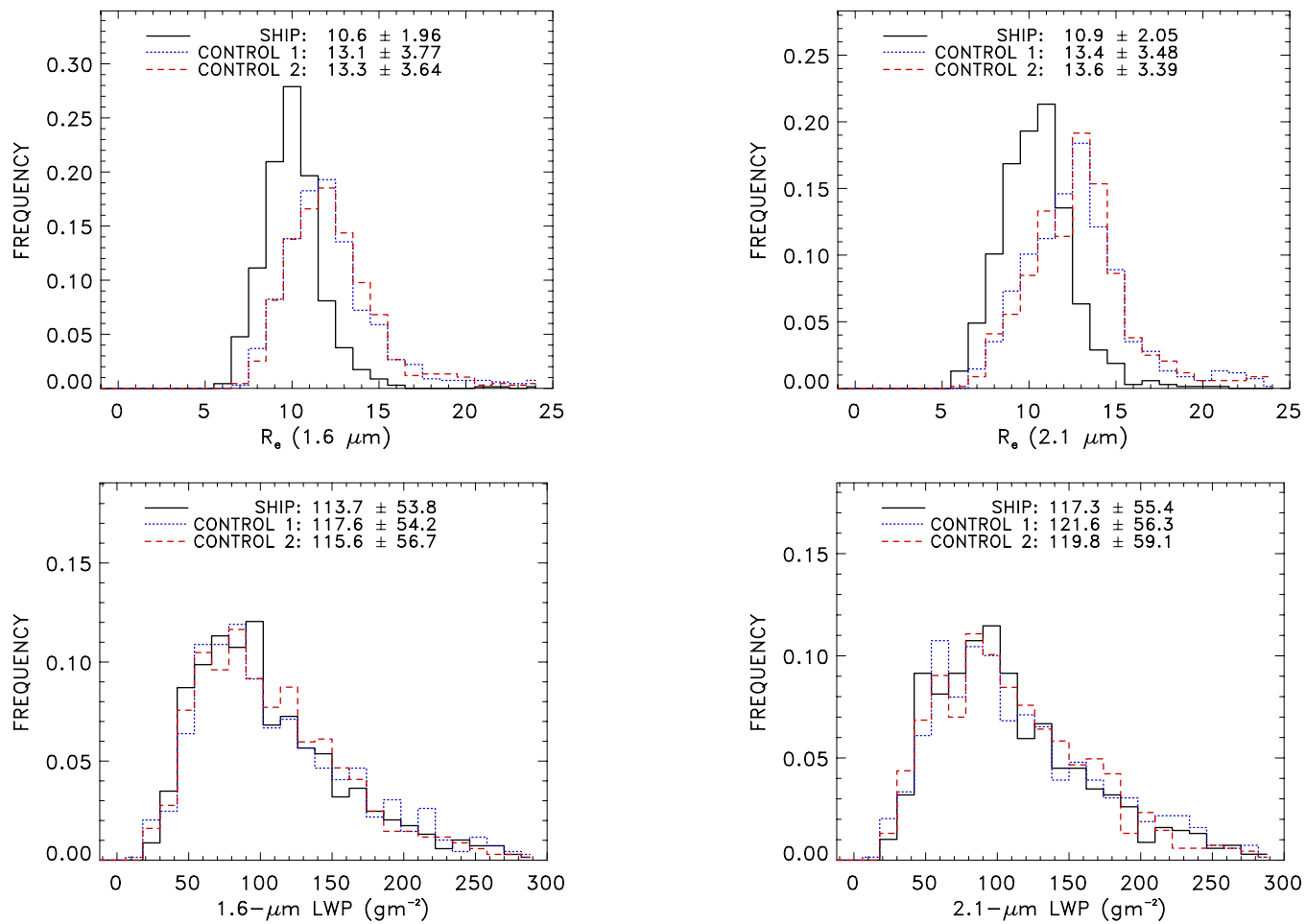


FIGURE 3.11. Same as figure 3.8 except for droplet effective radii and cloud liquid water paths derived using the 1.6 and 2.1- $\mu\text{m}$  channels.

TABLE 3.8. Means and standard deviation of the means for cloud optical depths, cloud droplet effective radii derived using the 1.6, 2.1, and 3.7- $\mu\text{m}$  channels, and the associated cloud liquid water paths for the ship track and controls. The difference between the ship and the controls and the rms of the standard deviation of the means is also shown for each of the cloud properties. N = number of track segments over which cloud properties were averaged.

N=694	$R_e$ ( $\mu\text{m}$ )			$\tau$	LWP ( $\text{gm}^{-2}$ )		
	1.6	2.1	3.7		1.6	2.1	3.7
Ship	$10.6 \pm 1.96$	$10.9 \pm 2.05$	$10.2 \pm 2.29$	$16.0 \pm 6.72$	$113.7 \pm 53.8$	$117.3 \pm 55.4$	$109.4 \pm 54.0$
Controls	$13.2 \pm 3.71$	$13.5 \pm 3.44$	$12.7 \pm 3.16$	$13.7 \pm 6.17$	$116.6 \pm 55.5$	$120.7 \pm 57.7$	$115.3 \pm 60.0$
Difference	$-2.6 \pm 2.97$	$-2.6 \pm 2.83$	$-2.5 \pm 2.76$	$2.3 \pm 6.45$	$-2.9 \pm 54.7$	$-3.4 \pm 56.6$	$-5.9 \pm 57.1$

TABLE 3.9. Means and standard error of the means for the differences between ship and controls and the differences between control 1 and control 2 for cloud optical depths, cloud droplet effective radii derived using the 1.6, 2.1, and 3.7- $\mu\text{m}$  channels, and the associated cloud liquid water paths. N = number of track segments over which cloud properties were averaged.

N=694	$R_e$ ( $\mu\text{m}$ )			$\tau$	LWP ( $\text{gm}^{-2}$ )		
	1.6	2.1	3.7		1.6	2.1	3.7
Ship – Controls	$-2.58 \pm 0.09$	$-2.59 \pm 0.08$	$-2.46 \pm 0.06$	$2.32 \pm 0.12$	$-2.86 \pm 0.91$	$-3.42 \pm 0.95$	$-5.92 \pm 0.95$
Control 1 – Control 2	$-0.16 \pm 0.08$	$-0.18 \pm 0.07$	$0.16 \pm 0.07$	$-0.32 \pm 0.13$	$-2.07 \pm 1.42$	$-1.88 \pm 1.47$	$-2.08 \pm 1.52$

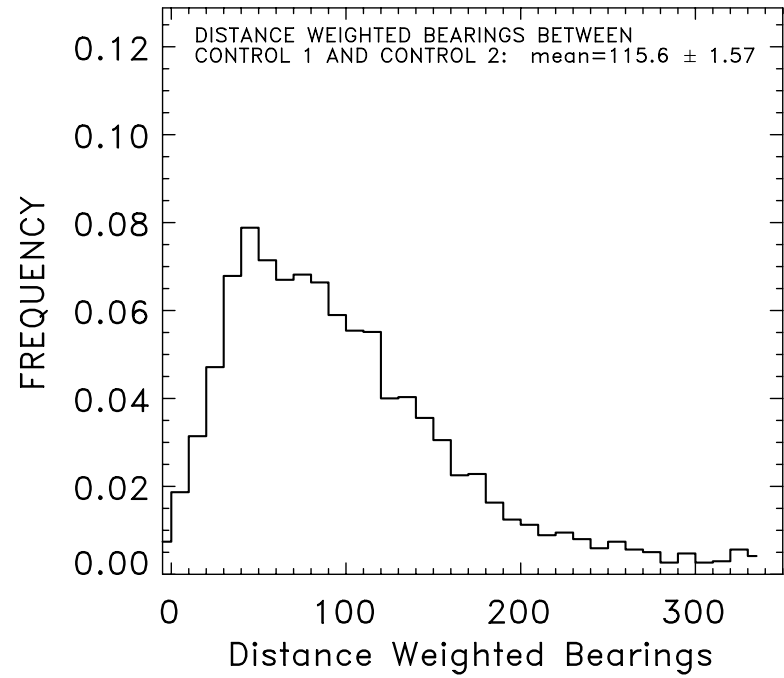
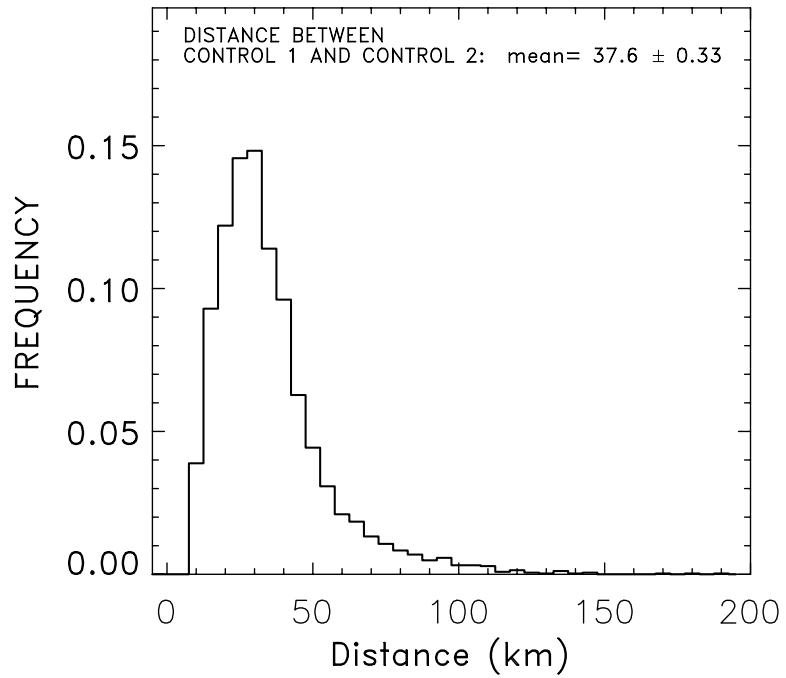


FIGURE 3.12. Average distance and the distance-weighted bearings. Means and standard error of the means are given.

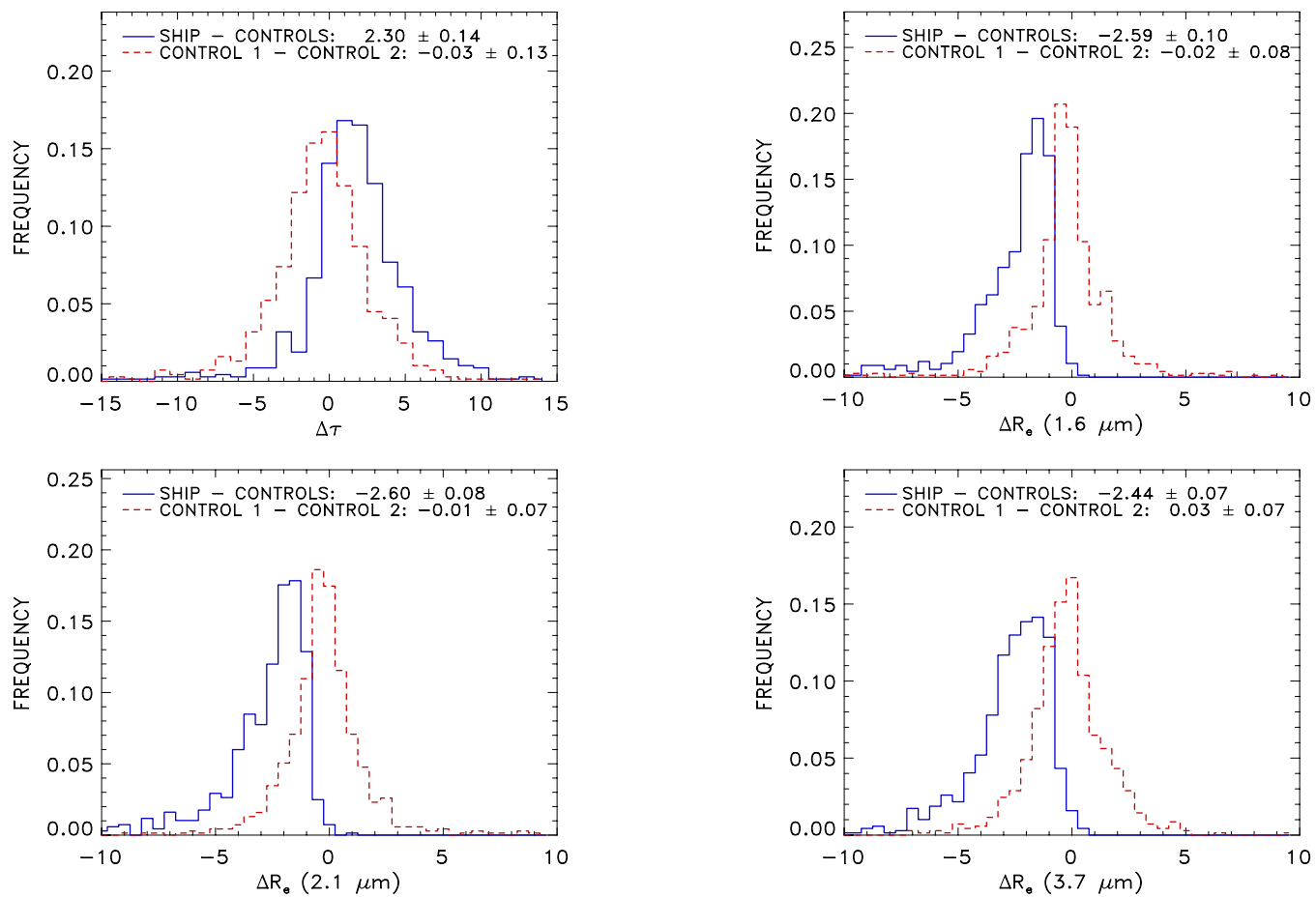


FIGURE 3.13. Mean differences between the ship and controls (solid blue line) and between control 1 and control 2 (dashed red line) for cloud optical depth, droplet effective radii derived using the 1.6, 2.1 and 3.7- $\mu\text{m}$  channels, and the associated cloud liquid water paths, for 20-pixel track segments. The means and standard error of the means are given.

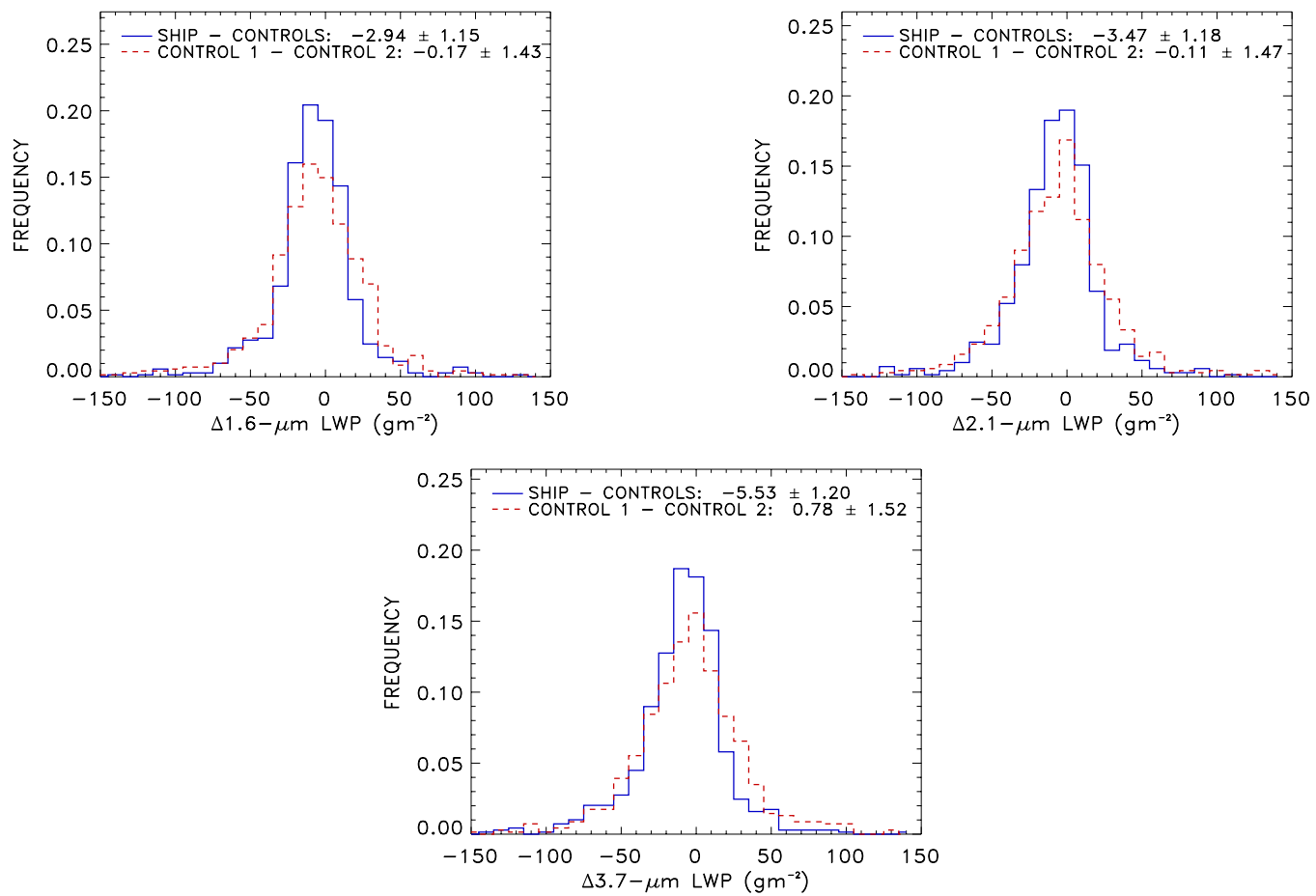


Figure 3.13. (Continued)

TABLE 3.10. Means for the differences between ship and controls along with the 99% confidence intervals for each of the cloud properties. N = number of track segments over which cloud properties were averaged.

N=694	$R_e$ ( $\mu\text{m}$ )			$\tau$	LWP ( $\text{gm}^{-2}$ )			$z_c$ (km)
	1.6	2.1	3.7		1.6	2.1	3.7	
Confidence Interval	$-2.59 \pm 0.23$	$-2.60 \pm 0.23$	$-2.44 \pm 0.23$	$2.30 \pm 0.35$	$-2.94 \pm 1.00$	$-3.74 \pm 1.07$	$-5.53 \pm 1.03$	$-0.01 \pm 0.11$

TABLE 3.11. Means and standard error of the means for the differences between ship and controls and the randomized differences between control 1 and control 2 for cloud optical depths, cloud droplet effective radii derived using the 1.6, 2.1, and 3.7- $\mu\text{m}$  channels, and the associated cloud liquid water paths. N = number of track segments over which cloud properties were averaged.

N=694	$R_e$ ( $\mu\text{m}$ )			$\tau$	LWP ( $\text{gm}^{-2}$ )		
	1.6	2.1	3.7		1.6	2.1	3.7
Ship – Controls	$-2.59 \pm 0.10$	$-2.60 \pm 0.08$	$-2.44 \pm 0.08$	$2.30 \pm 0.14$	$-2.94 \pm 1.15$	$-3.47 \pm 1.18$	$-5.53 \pm 1.20$
Control 1 – Control 2	$-0.02 \pm 0.08$	$-0.01 \pm 0.01$	$0.03 \pm 0.07$	$-0.03 \pm 0.27$	$-0.17 \pm 1.43$	$-0.11 \pm 1.47$	$0.78 \pm 1.52$

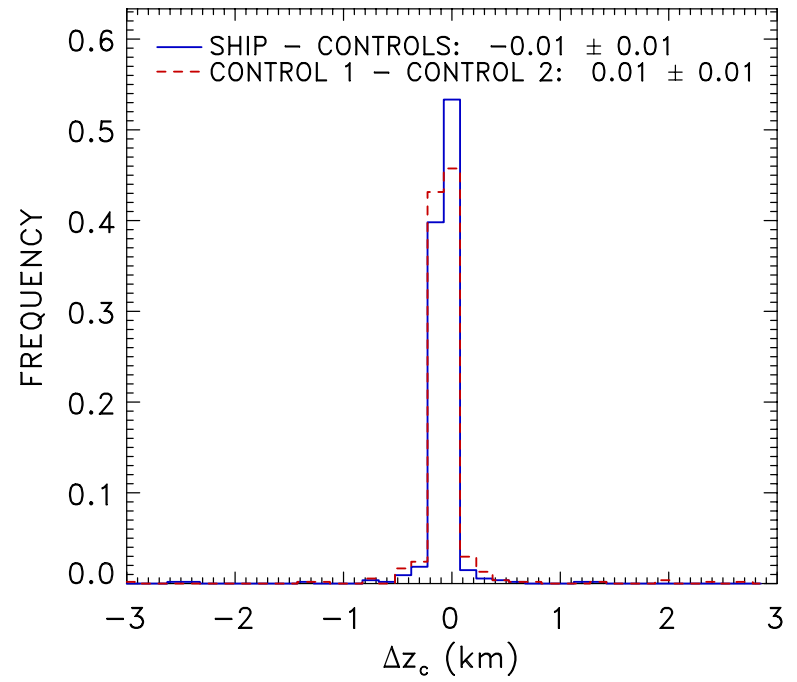
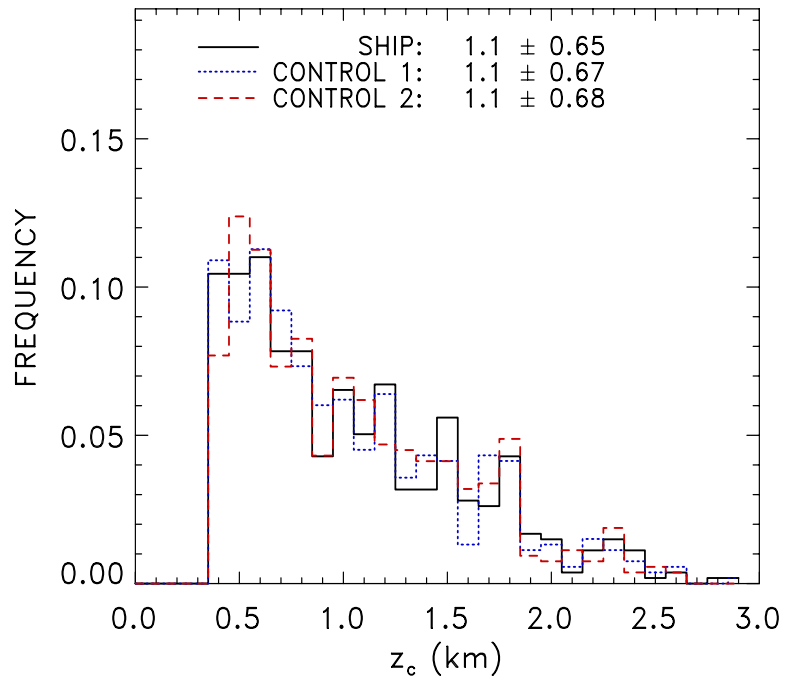


FIGURE 3.14. Same as figure 3.7 except for *Aqua* observations.

TABLE 3.12. Same as Table 3.6 except segments were kept only if they had changes in the droplet effective radii that were greater than or equal to  $2 \mu\text{m}$ .

$\Delta R_e \geq 2 \mu\text{m}$			
N=207	1.6 $\mu\text{m}$		
	$R_e (\mu\text{m})$	$\tau$	LWP ( $\text{gm}^{-2}$ )
Ship	$11.4 \pm 2.62$	$14.6 \pm 6.73$	$105.0 \pm 53.8$
Controls	$16.4 \pm 4.78$	$11.3 \pm 5.37$	$110.8 \pm 56.5$
Difference	$-5.0 \pm 3.85$	$3.3 \pm 6.09$	$-5.8 \pm 55.2$
N=234	2.1 $\mu\text{m}$		
	$R_e (\mu\text{m})$	$\tau$	LWP ( $\text{gm}^{-2}$ )
Ship	$11.6 \pm 2.21$	$15.1 \pm 6.90$	$110.9 \pm 55.7$
Controls	$16.1 \pm 3.92$	$11.8 \pm 5.61$	$115.4 \pm 55.4$
Difference	$-4.5 \pm 3.18$	$3.3 \pm 6.29$	$-4.5 \pm 55.6$
N=259	3.7 $\mu\text{m}$		
	$R_e (\mu\text{m})$	$\tau$	LWP ( $\text{gm}^{-2}$ )
Ship	$10.7 \pm 2.44$	$15.5 \pm 7.14$	$114.4 \pm 57.2$
Controls	$14.6 \pm 3.17$	$12.3 \pm 5.88$	$125.5 \pm 62.2$
Difference	$-3.9 \pm 2.83$	$3.2 \pm 6.54$	$-11.1 \pm 59.8$

TABLE 3.13. Same as Table 3.5 except for *Aqua* observations.

$\Delta R_e \geq 2 \mu\text{m}$			
N=207	1.6 $\mu\text{m}$		
	$\Delta R_e (\mu\text{m})$	$\Delta\tau$	$\Delta\text{LWP} (\text{gm}^{-2})$
Ship – Controls	$-5.03 \pm 0.22$	$3.16 \pm 0.22$	$-5.16 \pm 2.10$
Control 1 – Control 2	$-0.04 \pm 0.21$	$-0.02 \pm 0.19$	$1.16 \pm 2.36$
N=234	2.1 $\mu\text{m}$		
	$\Delta R_e (\mu\text{m})$	$\Delta\tau$	$\Delta\text{LWP} (\text{gm}^{-2})$
Ship – Controls	$-4.48 \pm 0.16$	$3.21 \pm 0.24$	$-5.21 \pm 2.23$
Control 1 – Control 2	$-0.02 \pm 0.15$	$0.06 \pm 0.19$	$-1.60 \pm 2.15$
N=259	3.7 $\mu\text{m}$		
	$\Delta R_e (\mu\text{m})$	$\Delta\tau$	$\Delta\text{LWP} (\text{gm}^{-2})$
Ship – Controls	$-3.94 \pm 0.10$	$3.09 \pm 0.28$	$-11.16 \pm 2.28$
Control 1 – Control 2	$-0.04 \pm 0.11$	$0.12 \pm 0.21$	$-0.24 \pm 2.38$

Table 3.14. Same as Table 10 except segments were kept only if they had changes in cloud droplet effective radii that were greater than or equal to  $2 \mu\text{m}$ .

$\Delta R_e \geq 2 \mu\text{m}$			
N=207	1.6 $\mu\text{m}$		
	$R_e (\mu\text{m})$	$\tau$	LWP ( $\text{gm}^{-2}$ )
Confidence Interval	$-5.03 \pm 0.48$	$3.16 \pm 0.62$	$-5.16 \pm 1.86$
N=234	2.1 $\mu\text{m}$		
	$R_e (\mu\text{m})$	$\tau$	LWP ( $\text{gm}^{-2}$ )
Confidence Interval	$-4.87 \pm 0.41$	$3.21 \pm 0.59$	$-5.21 \pm 1.75$
N=259	3.7 $\mu\text{m}$		
	$R_e (\mu\text{m})$	$\tau$	LWP ( $\text{gm}^{-2}$ )
Confidence Interval	$-3.94 \pm 0.37$	$3.09 \pm 0.57$	$-11.16 \pm 1.72$

### 3.3 Comparing *Terra* observations with *Aqua* observations

Several interesting observations arise when observations from *Terra* are compared with those from *Aqua*. First, the droplet effective radii for *Terra* and *Aqua* were nearly identical for both the polluted and unpolluted clouds. The cloud optical depths for the *Aqua* observations were significantly smaller than those of the *Terra* observations. Consequently, the liquid water paths for the *Aqua* observations were significantly smaller than those for the *Terra* observations. With droplet effective radii essentially the same for the morning and afternoon clouds, and liquid water decreasing, the most obvious explanation for the smaller optical depths and cloud liquid water amounts for the *Aqua* observations is that the afternoon clouds were thinner than the morning clouds. Marine stratiform clouds would be expected to respond in this way to solar heating and the evaporation of droplets. For the *Terra* observations cloud top height,  $z_c$ , averaged 1.3 km compared to the *Aqua* observations where  $z_c$  averaged 1.1 km. At the same time, the lifting condensation level (LCL), which sets the base of the cloud, is rising. The LCL occurs at the saturation point for air lifted adiabatically (Wallace and Hobbs, 1977). Since clouds cannot form below the LCL, solar heating would also cause the cloud to thin through the heating of the subcloud air and the rise in the LCL. Consequently, solar heating causes clouds to thin from both the top and bottom. These results are consistent with the thinning of the clouds as the day progresses.

When segments for which the changes in droplet effective radii were greater than  $2 \mu\text{m}$  were considered, responses in both the *Aqua* and *Terra* droplet effective radii were 25 to 30% larger and those for cloud optical depths were ~20% larger. The

percent loss in cloud liquid water paths, ~12 % for *Terra* and ~9% for *Aqua*, however, were still less than 15%, much smaller than the ~20% reduction found with the AVHRR observations (Coakley and Walsh, 2002). Comparing the *Terra* and *Aqua* observations, however, showed that cloud liquid water paths for the *Aqua* observations were much less than those for the *Terra* observations. Entrainment of dry air above the clouds coupled with solar heating thinning the clouds, from the top and from the cloud base, could explain why the *Aqua* observations showed smaller cloud liquid water paths compared with the *Terra* observations.

The question that arises next is, when changes in droplet effective radii were greater than 2  $\mu\text{m}$ , why did the Coakley and Walsh (2002) study find ~20% reduction in cloud liquid water and the results in this study find a reduction less than 15%. One possible reason for the difference is that the two studies used different satellites. The Coakley and Walsh (2002) study used National Oceanic and Atmospheric Administration (NOAA) satellite *NOAA-14* 1-km AVHRR observations and this study used National Aeronautics and Space Administration (NASA) satellites *Terra* and *Aqua* 1-km MODIS observations. The *Terra* and *Aqua* satellites passed over the region at 1030 and 1330 nominal local times respectively, much earlier than the 1600 nominal local time for the *NOAA-14* satellite. Much more solar heating had taken place with the *NOAA-14* observations which could easily affect the reduction in cloud liquid water. Another possibility for the difference between the two studies is the methodology used to retrieve the cloud properties and identify the ship track and control pixels. Unpolluted pixels in this study were much closer to pixels identified as being polluted compared to the Coakley and Walsh study. Furthermore, cloud

properties for this study included retrievals of cloud altitudes (Coakley et al., 2005), whereas in the Coakley and Walsh study the retrieval scheme fixed the altitudes at 1 km. The effects of these differences remain to be studied.

### 3.4 Statistical Independence

To ensure that sampling errors were well characterized by the method used to estimate them, an ensemble was created in which adjacent track segments were removed so that there was at least a 20-pixel separation measured along the track between the segments that were analyzed. This separation was imposed to avoid any spatial correlations that might arise among the cloud properties thereby violating the assumption that the segments represented independent samples. Of the remaining segments that were not removed, one-third of the segments were randomly chosen to be analyzed to check for statistical independence of the samples. For *Terra* 250 segments and for *Aqua* 231 segments were analyzed. Tables 3.15 and 3.16 show the results for the *Terra* and *Aqua* sampled ensembles. The means and standard error of the means for the ship track and control pixels are given for the cloud visible optical depth, cloud droplet effective radii derived using the 1.6, 2.1, and 3.7- $\mu\text{m}$  channels, and the associated cloud liquid water paths. In Tables 3.15 and 3.16 the means and standard errors were combined for the control 1 and control 2 pixels. The differences between the ship track and the control pixels and the rms of the standard errors are also given.

Based on the results listed in Tables 3.15 and 3.16, the mean cloud optical depths for the ship track pixels were greater than the mean cloud optical depths for the

control pixels and this difference was statistically significant. Moreover, the mean droplet effective radii for the ship track pixels were smaller than in the nearby control pixels by 2.4 – 2.9  $\mu\text{m}$  and these differences were, of course, highly significant. Once again, the 2.1- $\mu\text{m}$  droplet effective radius was slightly larger than the 1.6 and 3.7- $\mu\text{m}$  droplet effective radius, but the differences were within the errors anticipated for such retrievals (Nakajima and King, 1990). Additionally, the smaller cloud droplets in the ship track pixels coincided with the larger optical depths. Furthermore, it is evident that there was less liquid water in the ship track pixels compared to nearby control pixels based on the results for all the near infrared channels. The ship track pixels had approximately 6 – 11  $\text{gm}^{-2}$  less liquid water than the control pixels. The difference in the cloud liquid water was larger for the droplet effective radii derived using the 2.1- $\mu\text{m}$  channel than for the 1.6- $\mu\text{m}$  channel, and larger still for the droplet effective radii derived using the 3.7- $\mu\text{m}$  channel than for the 2.1- $\mu\text{m}$  channel.

Comparing the results in Tables 3.15 and 3.16 with those obtained using all the overcast segments, Tables 3.1 and 3.8, no significant differences were found. The cloud optical depths differed only a few tenths, the droplet effective radii were either the same or differed by  $\sim 0.3 \mu\text{m}$ , and the liquid water paths differed by only  $\sim 2 - 4 \text{ gm}^{-2}$ . All of these differences fell within the estimated uncertainties. By reducing the number of segments to one-third and analyzing only segments that were separated from their neighbors, the means were identical and uncertainties grew by approximately a factor of  $\sqrt{3}$ . The growth in uncertainty was expected given the reduction in sample size. Therefore, the results of the complete analysis of all

overcast segments and the estimates of the statistical uncertainty can be trusted and the assumption of independent samples is correct.

Terra

TABLE 3.15. Same as table 3.1 except there was at least a 20-pixel separation measured along the ship track between the segments, and of the remaining segments a third were randomly chosen to be analyzed.

N=250	$R_e$ ( $\mu\text{m}$ )			$\tau$	LWP ( $\text{gm}^{-2}$ )		
	1.6	2.1	3.7		1.6	2.1	3.7
Ship	$10.5 \pm 0.12$	$11.2 \pm 0.15$	$10.2 \pm 0.14$	$18.3 \pm 0.46$	$126.8 \pm 3.43$	$136.3 \pm 3.82$	$124.7 \pm 3.60$
Controls	$13.4 \pm 0.31$	$14.3 \pm 0.30$	$12.8 \pm 0.22$	$16.3 \pm 0.47$	$135.2 \pm 3.96$	$145.7 \pm 4.35$	$136.0 \pm 4.41$
Difference	$-2.9 \pm 0.24$	$-3.1 \pm 0.24$	$-2.6 \pm 0.18$	$2.0 \pm 0.47$	$-8.40 \pm 3.70$	$-8.61 \pm 4.09$	$-11.0 \pm 4.03$

Aqua

TABLE 3.16. Same as table 3.6 except there was at least a 20-pixel separation measured along the ship track between the segments, and of the remaining segments a third were randomly chosen to be analyzed.

N=231	$R_e$ ( $\mu\text{m}$ )			$\tau$	LWP ( $\text{gm}^{-2}$ )		
	1.6	2.1	3.7		1.6	2.1	3.7
Ship	$10.7 \pm 0.13$	$11.1 \pm 0.14$	$10.4 \pm 0.15$	$15.4 \pm 0.41$	$109.9 \pm 3.26$	$114.7 \pm 3.45$	$107.5 \pm 3.37$
Controls	$13.4 \pm 0.28$	$13.8 \pm 0.24$	$12.8 \pm 0.21$	$13.5 \pm 0.40$	$116.3 \pm 3.67$	$120.7 \pm 3.84$	$115.3 \pm 3.97$
Difference	$-2.7 \pm 0.22$	$-2.7 \pm 0.20$	$-2.4 \pm 0.18$	$1.9 \pm 0.41$	$-6.4 \pm 3.47$	$-6.0 \pm 3.65$	$-7.8 \pm 3.68$

## CHAPTER 4

### CLOUD SENSITIVITY

The results for the *Terra* and *Aqua* observations prompt the following questions: 1) Which clouds were the most sensitive? 2) Why were these particular clouds the most sensitive? Answers to these questions may come from the work of Platnick and Twomey (1994) on cloud susceptibility. According to Platnick and Twomey (1994), cloud susceptibility is the increase in cloud albedo resulting from the addition of one cloud droplet per cubic centimeter, keeping cloud liquid water constant. Susceptibility is a function of droplet radius and cloud optical depth. Clean clouds will be more susceptible than polluted clouds. Clean clouds have fewer, but larger, droplets compared to polluted clouds that have more, but smaller, droplets. Platnick and Twomey (1994) suggested that marine stratiform clouds, such as those in this study, will have larger variations in susceptibilities, on small scales, due to their relatively large droplets and small optical depths. They also suggested that polluted clouds, such as ship tracks, were less susceptible than unpolluted clouds.

A major constraint in the Platnick and Twomey definition of cloud susceptibility was that cloud liquid water remained constant. For the most part, marine stratiform clouds polluted by underlying ships lost liquid water. Since liquid water decreased, instead of analyzing cloud susceptibility, this study characterized the clouds that were most sensitive to change by underlying ships. In other words, which clouds were the most sensitive to changes in cloud albedo regardless if cloud liquid

water did not remain constant. Based on the Eddington approximation, the reflectance,  $r$ , or cloud albedo, can be defined as

$$r = \frac{\frac{3}{4}(1-g)\tau}{1 + \frac{3}{4}(1-g)\tau} = \frac{\beta\tau}{1 + \beta\tau} \quad (3.1)$$

where  $\beta = \frac{3}{4}(1-g)$ ,  $\tau$  is the optical depth of the clouds, and  $g$  is the asymmetry factor.  $g > 0$  represents scattering that is peaked in the forward direction, and  $g < 0$  represents scattering that is peaked in the direction of backscatter.  $\beta$  and  $g$  are weak functions of cloud droplet effective radius. At  $0.64 \mu\text{m}$ ,  $g$  ranges from 0.792 to 0.883 as droplet effective radius ranges from 2 to  $40 \mu\text{m}$ . The change in reflectance is given by

$$\begin{aligned} \Delta r &= \frac{\beta\Delta\tau}{1 + \beta\tau} - \frac{\beta^2\tau\Delta\tau}{(1 + \beta\tau)^2} \\ &= \frac{\beta\Delta\tau(1 + \beta\tau)}{(1 + \beta\tau)(1 + \beta\tau)} - \frac{\beta^2\tau\Delta\tau}{(1 + \beta\tau)^2} \\ &= \frac{\beta\Delta\tau}{(1 + \beta\tau)^2} \\ &= \left( \frac{\beta\tau}{1 + \beta\tau} \right) \left( \frac{1}{1 + \beta\tau} \right) \left( \frac{\Delta\tau}{\tau} \right) \end{aligned}$$

$$\text{Therefore, } \Delta r = r(1-r)\frac{\Delta\tau}{\tau} \quad (3.2)$$

Figure 4.1 shows the distribution of changes in cloud reflectance for *Terra* and *Aqua* observations. Means and the standard error of the means are given. The negative

change in the reflectances indicates that in some cases the clouds in the control pixels had larger optical depths, and thus larger reflectances, than the clouds in ship track pixels. Often reflectances for the control pixels were greater than those of the ship track pixels near the tail of the track where considerable mixing between polluted and unpolluted clouds had occurred. The ship track itself, however, was still detectable in the 2.1- $\mu\text{m}$  reflectances used by the automated identification scheme. The results in Fig. 4.1 suggest that the changes in cloud reflectances for the *Aqua* observations were slightly larger than those for the *Terra* observations. The afternoon clouds were slightly more sensitive than the morning clouds. These differences, however, were at the detection limit. Figure 4.2 shows changes in cloud reflectances ( $\Delta r$ ) for the *Terra* and *Aqua* observations and the fractional change in cloud optical depth  $\left(\frac{\Delta\tau}{\tau}\right)$ . For the range of cloud optical depths and droplet effective radii in this study, the change in reflectance was strongly proportional to  $\frac{\Delta\tau}{\tau}$ . Therefore,  $\frac{\Delta\tau}{\tau}$  will be used as a proxy for the change in reflectance.

Figure 4.3 shows fractional change in cloud optical depth for various droplet effective radii derived using the 3.7- $\mu\text{m}$  channel and cloud optical depths, for the *Terra* observations. The results in Fig. 4.3 suggest that fractional changes in cloud optical depths were small for most clouds. The clouds with the smaller optical depths and larger droplet effective radii were the clouds that had the largest fractional changes in optical depth. Conversely, clouds that had larger optical depths and smaller droplet effective radii were the clouds that demonstrated little change in cloud

reflectances. These findings are shown for *Aqua* observations in Figure 4.4. As with the *Terra* observations, the clouds that had the smaller cloud optical depths and larger droplet effective radii were the clouds that had the largest fractional changes in optical depths, and clouds with larger optical depths and smaller droplet effective radii were the clouds with the smallest fractional changes in optical depth. For both morning and afternoon clouds, those with the smaller optical depths and larger droplet effective radii were the clouds with reflectances that exhibited the most sensitivity to change.

Why were the clouds that had the smaller optical depths and larger droplet effective radii the most sensitive? Figure 4.5 shows the changes in cloud liquid water paths for values of the droplet effective radii derived using the 3.7- $\mu\text{m}$  channel and cloud optical depths. Cloud liquid water path is given by  $LWP = \frac{2}{3} \tau_c R_e \rho$ . To first order, the fractional change in cloud liquid water path is given by the sum of the fractional changes in droplet effective radius and cloud optical depth. Based on the results shown in Fig. 4.5 most clouds lose liquid water. Only clouds with small optical depths and large droplet effective radii gain liquid water. These findings are echoed in the *Aqua* observations shown in Figure 4.6. Therefore, for both morning and afternoon, the clouds that had the largest increase in reflectances also had increases in cloud liquid water. They were clouds which had small optical depths and large droplet effective radii.

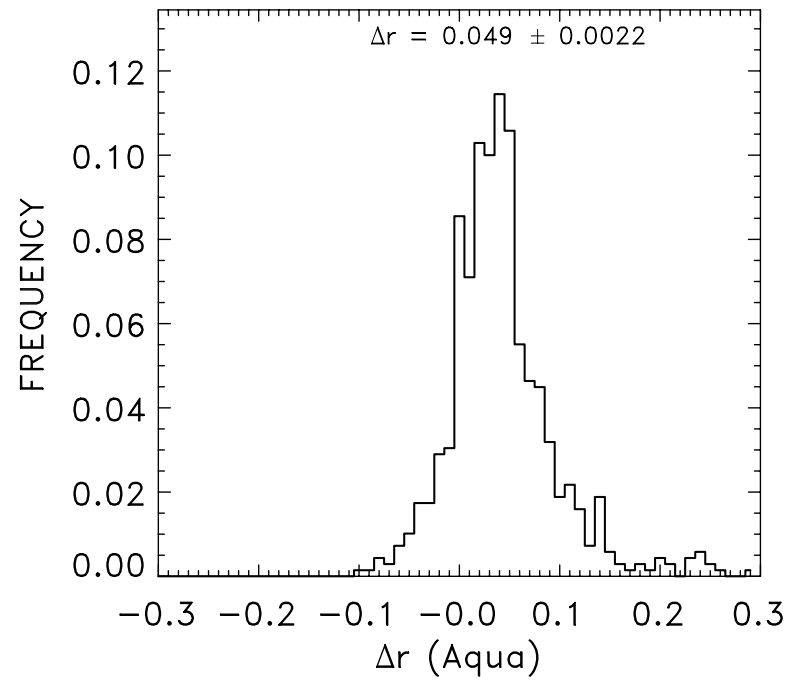
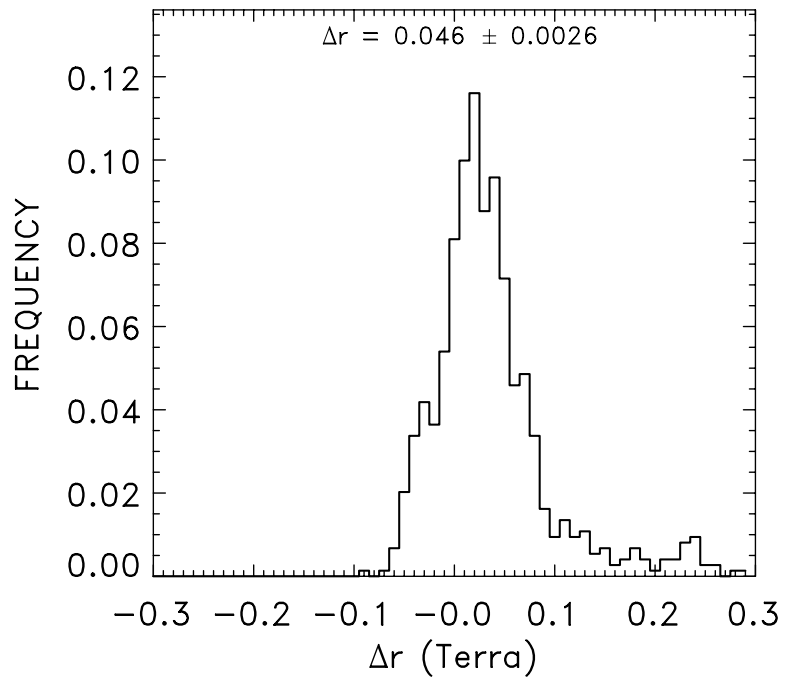


FIGURE 4.1. Distribution of changes in reflectance for *Terra* and *Aqua* observations. The means and standard error of the means are given.

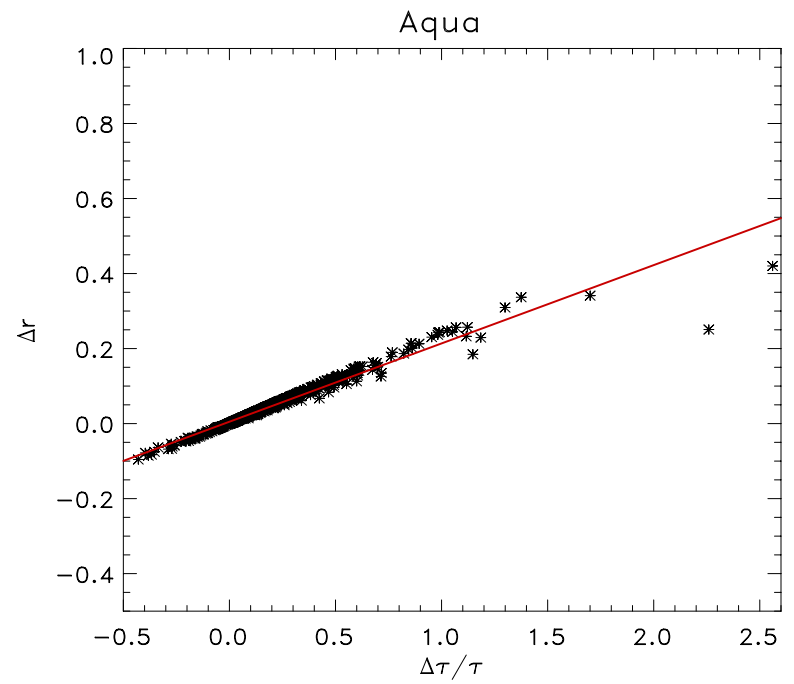
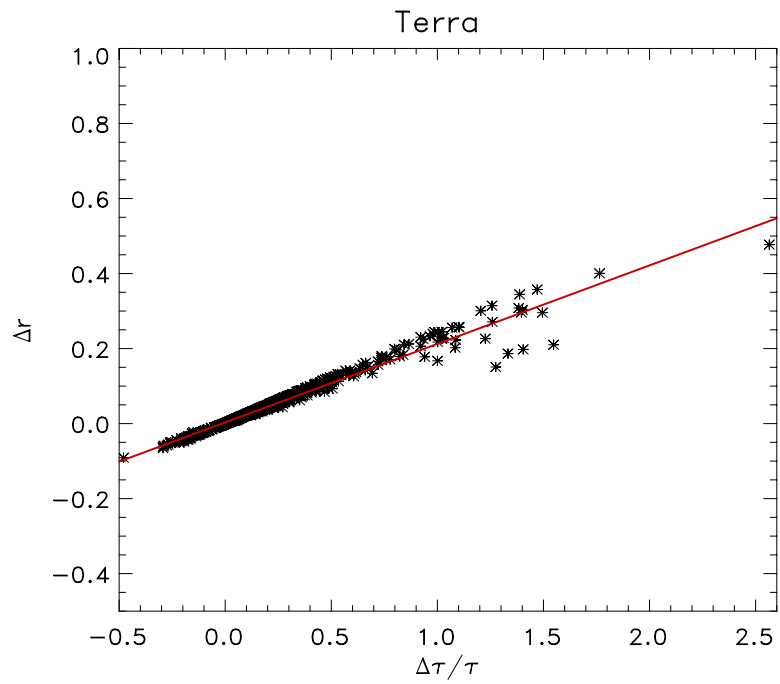


FIGURE 4.2. Change in cloud reflectance and fractional change in cloud optical depth.

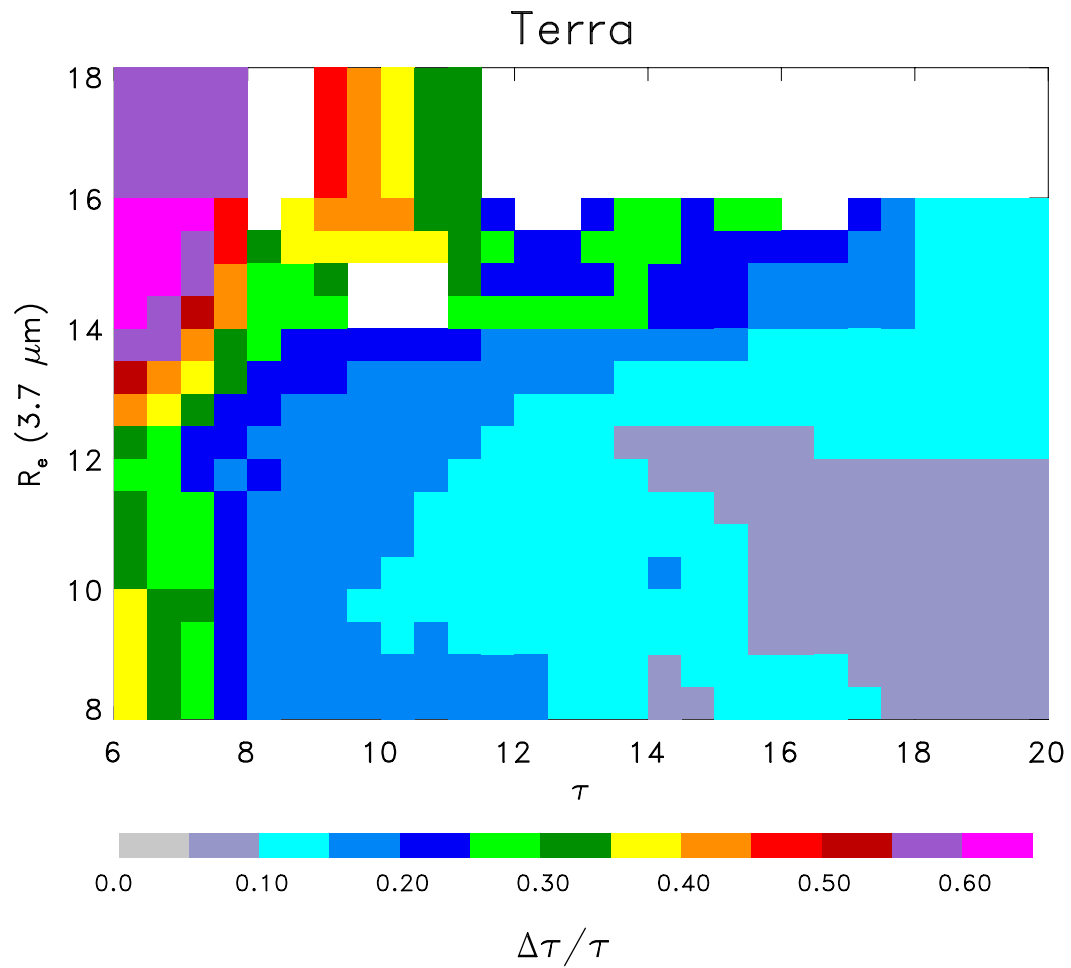


FIGURE 4.3. Fractional change in optical depth for droplet effective radii and cloud optical depths associated with the control pixels. The observations are for the *Terra* MODIS. The fractional change in optical depth is used as a proxy for the change in cloud albedo.

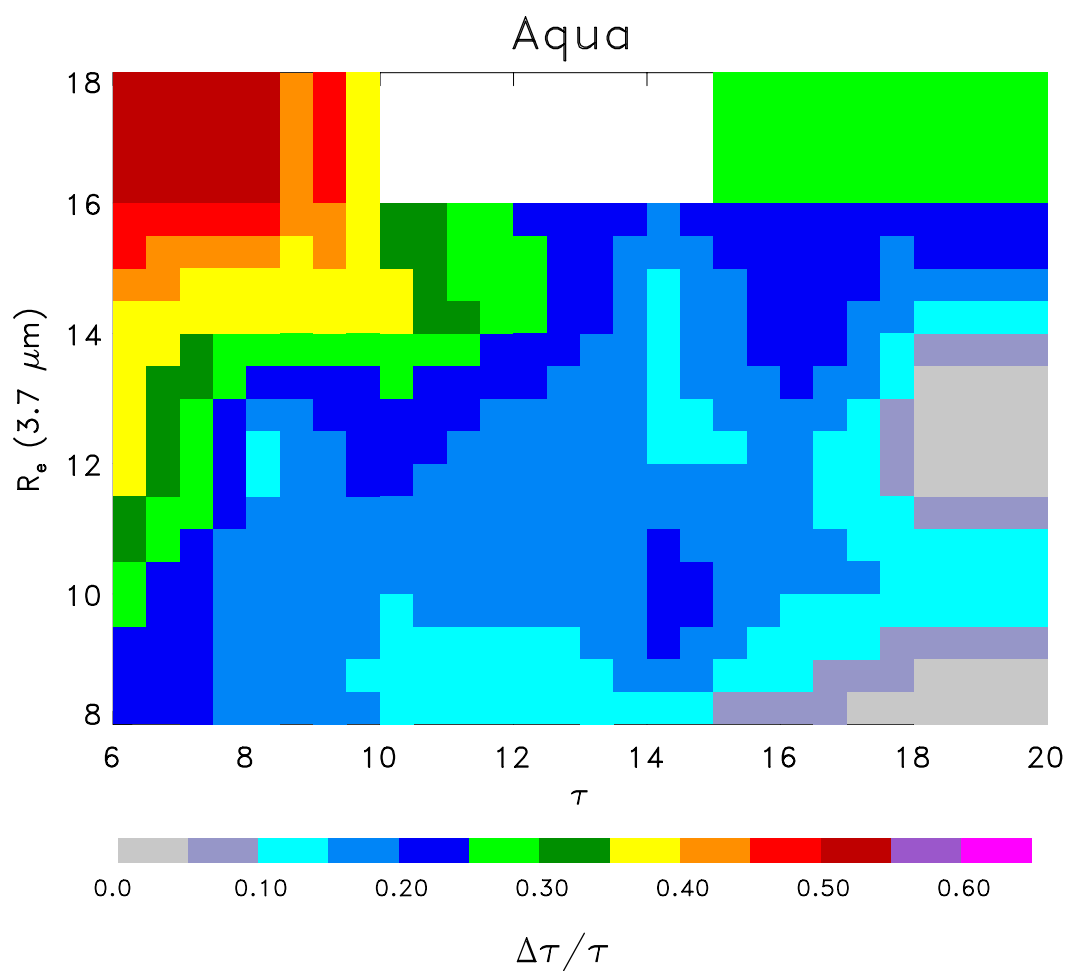


FIGURE 4.4. Same as figure 4.3 except for *Aqua* observations.

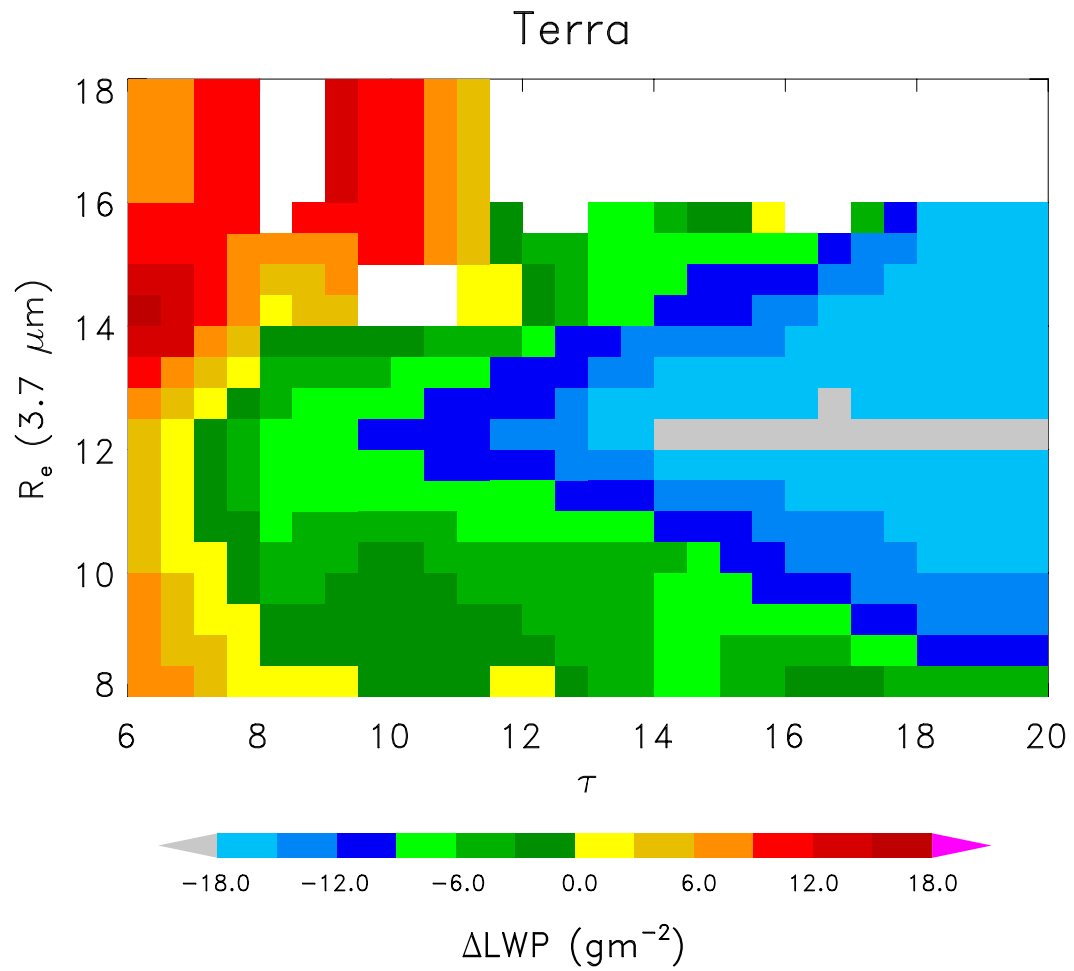


FIGURE 4.5. Changes in cloud liquid water paths for droplet effective radii and cloud optical depths associated with the control pixels. The observations are for the *Terra* MODIS.

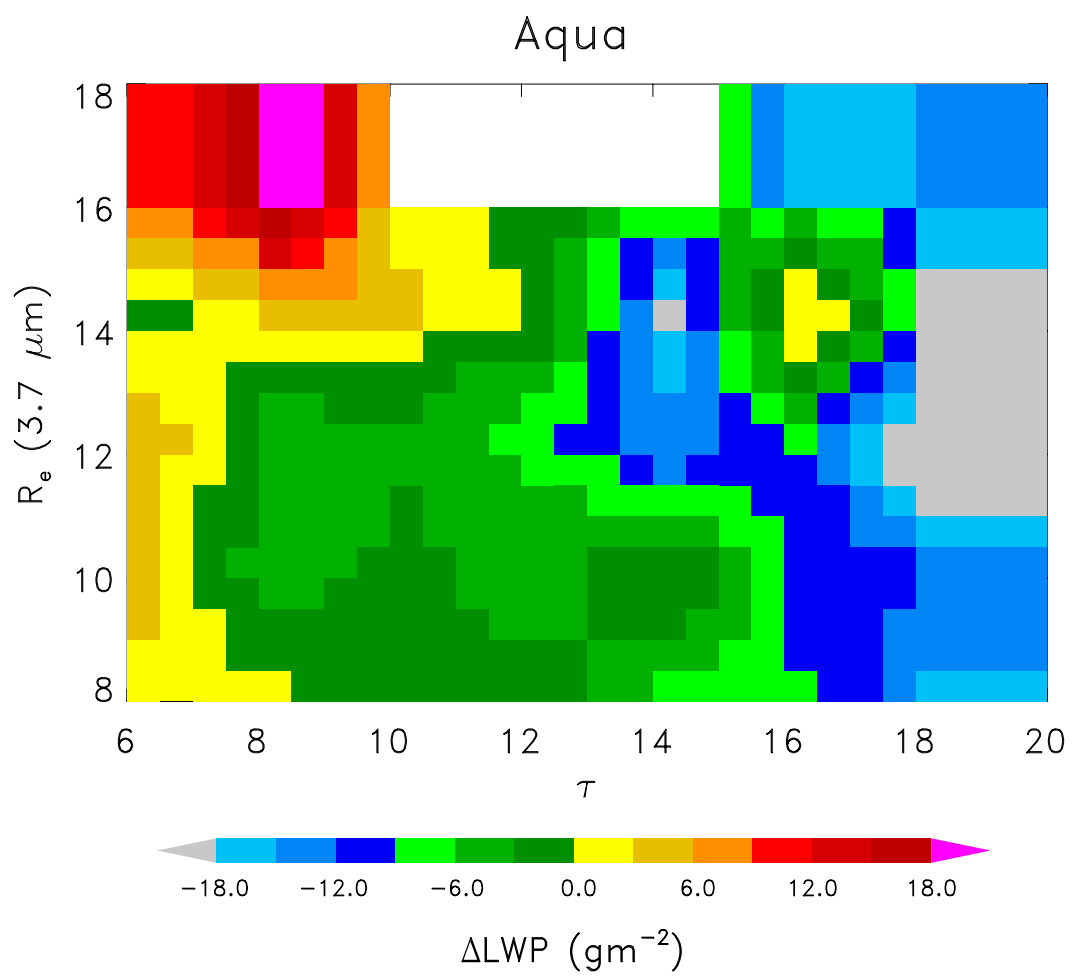


FIGURE 4.6. Same as figure 4.5 except for *Aqua* observations.

## CHAPTER 5

### CONCLUSIONS

1-km MODIS imagery were collected over the northeastern Pacific for the *Terra* satellite, May – August, 2001 – 2003, and for the *Aqua* satellite, June – August, 2002, and May – August, 2003 – 2004. The 11- $\mu\text{m}$  imagery was used to identify single-layered, low-level cloud layers, and the 2.1 and 3.7- $\mu\text{m}$  images were used to identify ship tracks. Over 4200 ship tracks were logged by hand within the geographic region chosen for analysis. The ship tracks were used to characterize the effects of haze particles on clouds. Using the hand logged positions of the ship tracks, an automated track finding scheme identified pixels that contained clouds polluted by the ship and then selected control pixels on either side of the track that contained unpolluted clouds.

Analysis of the *Terra* and *Aqua* observations revealed that droplet effective radii for polluted pixels were significantly smaller than droplet effective radii for unpolluted pixels. Additionally, cloud optical depths for polluted pixels were significantly larger than those for unpolluted pixels. For the *Terra* observations, cloud liquid water paths were found to have ~5 – 8% less liquid water in the polluted pixels compared with the unpolluted pixels, and in the *Aqua* observations polluted clouds had less liquid water by ~2.5 – 5% compared with unpolluted clouds. For the ensemble of cases in which the change in droplet effective radius was greater than or equal to 2  $\mu\text{m}$ , droplet effective radii and cloud optical depths showed significant differences between the polluted and unpolluted pixels. The cloud liquid water paths for the

polluted clouds in the *Terra* observations were now ~8 – 13% less, and the polluted clouds in the *Aqua* observations had ~5 – 9% less liquid water compared with unpolluted clouds. These percent differences were much smaller than the ~20% reduction in cloud liquid water paths found with AVHRR observations (Coakley and Walsh, 2002). Comparing the *Terra* and *Aqua* observations, the cloud liquid water paths for the *Aqua* observations were much less than those for the *Terra* observation and this was most likely due to the effects of solar heating. Furthermore, the average cloud top height for the *Terra* observations was 1.3 km and for the *Aqua* observations was 1.1 km. These results were consistent with the thinning of clouds due to the evaporation of droplets by solar heating.

To ensure that the assumption of independent samples was correct, an ensemble was created in which adjacent track segments were removed so that there was at least a 20-pixel separation measured along the ship track between segments used in the analysis. A third of the remaining segments were randomly chosen to be analyzed to further ensure the statistical independence of the analyzed samples. The results showed that the means were the same and uncertainties grew as would be expected for independent samples. The assumption that the samples were statistically independent proved to be reasonable.

Which clouds were most sensitive to change and why these particular clouds were the most sensitive was also investigated. For both the *Terra* and *Aqua* observations, the clouds that displayed the largest changes in cloud reflectances were clouds with small optical depths and large droplet effective radii. These were the same clouds in which liquid water increased when the clouds were polluted.

Therefore, for morning and afternoon, the clouds that had the largest increase in reflectances also had increases in cloud liquid water and were the clouds which had small optical depths and large droplet effective radii.

## Bibliography

- Ackerman, A. S., O. B. Toon, and P. V. Hobbs, 1995: Numerical modeling of ship tracks produced by injection of cloud condensation nuclei into marine stratiform clouds. *J. Geophys. Res.*, **100**, 7121-7133.
- Ackerman, A. S., M. P. Kirkpatrick, D. E. Stevens, and O. B. Toon, 2004: The impact of humidity above stratiform clouds on indirect aerosol climate forcing. *Nature*, **432**, 1014-1017.
- Albrecht, B. A. 1989: Aerosols, cloud microphysics and fractional cloudiness. *Science*, **245**, 1227-1230.
- Breon, F. M., D. Tanre, and S. Generoso. 2002: Aerosol effect on cloud droplet size monitored from satellite. *Science*, **295**, 834-838.
- Coakley, J. A., Jr., R.L. Bernstein, and P. A. Durkee, 1987: Effect of ship-stack effluents on cloud reflectivity. *Science*, **237**, 1020-1022.
- Coakley, J. A., Jr., and C. D. Walsh, 2002: Limits to the aerosol indirect radiative effect derived from observations of ship tracks. *J. Atmos. Sci.*, **59**, 668-680.
- Coakley, J. A. Jr., M. A. Friedman, and W. R. Tahnk, 2005: Retrieval of cloud properties for partly cloudy imager pixels. *J. Atmos. Oce. Tech.*, **22**, 3-17.
- Conover, J. H., 1966: Anomalous cloud lines. *J. Atmos. Sci.*, **23**, 778-785.
- Durkee, P. A., K. J. Noone, and R. T. Bluth, 2000: The Monterey Area Ship Track Experiment. *J. Atmos. Sci.*, **57**, 2523-2541.
- Durkee, P. A., K. J. Noone, R. J. Ferek, D. W. Johnson, J. P. Taylor, T. J. Garrett, P. V. Hobbs, J. G. Hudson, C. S. Bretherton, G. Innis, G. M. Frick, W. A. Hoppel, C. D. O'Dowd, L. M. Russell, R. Gasparovic, K. E. Nielsen, S. A. Tessmer, E. Ostrom, S. R. Osborne, R. C. Flagan, J. H. Seinfeld, and H. Rand, 2000: The impact of ship-produced aerosols on the microstructure and albedo of warm marine stratocumulus clouds: A test of MAST hypotheses 1i and 1ii. *J. Atmos. Sci.*, **57**, 2554-2569.
- Ferek, R. J., T. Garrett, P. V. Hobbs, S. Strader, D. Johnson, J. P. Taylor, K. Nielsen, A. S. Ackerman, Y. Kogan, Q. Liu, B. A. Albrecht, and D. Babb, 2000: Drizzle suppression of ship tracks. *J. Atmos. Sci.*, **57**, 2707-2728.

- Hobbs, P. V., T. J. Garrett, R. J. Ferek, S. R. Strader, D. A. Hegg, G. M. Frick, W. A. Hoppel, R. F. Gasparovic, L. M. Russell, D. W. Johnson, C. O'Dowd, P. A. Durkee, K. E. Nielsen, and G. Innis, 2000: Emissions from ships with respect to their effects on clouds. *J. Atmos. Sci.*, **57**, 2570-2590.
- Intergovernmental Panel on Climate Change (IPCC), 2001: *Climate Change 2001: The Scientific Basis*, edited by J. T. Houghton et al., Cambridge Univ. Press, New York, New York.
- Lohmann, U., and J. Feichter, 1997: Impact of sulfate on albedo and lifetime of clouds: A sensitivity study with the ECHAM4 GCM. *J. Geophys. Res.*, **102**, 13685-13700.
- Matheson, M. A., J. A. Coakley Jr., and W. R. Tahnk, 2005: Aerosol and cloud property relationships for summertime stratiform clouds in the northeastern Atlantic from Advanced Very High Resolution Radiometer observations. *J. Geophys. Res.*, **110**, D24204.
- Nakajima, T., and M. D. King, 1990: Determination of the optical thickness and effective particle radius of clouds from reflected solar radiation measurements. Part I: theory. *J. Atmos. Sci.*, **47**, 1878-1893.
- Noone, K. J., E. Ostrom, R. J. Ferek, T. Garrett, P. V. Hobbs, D. W. Johnson, J. P. Taylor, L. M. Russell, R. C. Flagan, J. H. Seinfeld, C. D. O'Dowd, M. H. Smith, P. A. Durkee, K. Nielsen, J. G. Hudson, R. A. Pockalny, L. D. Bock, R. E. Van Grieken, R. F. Gasparovic, and I. Brooks, 2000a: A case study of ships forming and not forming tracks in moderately polluted clouds. *J. Atmos. Sci.*, **57**, 2729-2747.
- Noone, K. J., D. W. Johnson, J. P. Taylor, R. J. Ferek, T. Garrett, P. V. Hobbs, P. V. Durkee, K. Nielsen, E. Ostrom, C. O'Dowd, M. H. Smith, L. M. Russell, R. C. Flagan, J. H. Seinfeld, L. D. Bock, R. E. Van Grieken, J. G. Hudson, I. Brooks, R. F. Gasparovic, and R. A. Pockalny, 2000b: A case study of ship track formation in a polluted marine boundary layer. *J. Atmos. Sci.*, **57**, 2748-2763.
- Platnick, S. P., and S. Twomey, 1994: Determining the susceptibility of cloud albedo to changes in droplet concentration with the Advanced Very High Resolution Radiometer. *J. Appl. Meteor.*, **33**, 334-347.
- Platnick, S., P. A. Durkee, K. Nielsen, J. P. Taylor, S.-C. Tsay, M. D. King, R. J. Ferek, P. V. Hobbs, and J. W. Rottman, 2000: The role of background cloud microphysics in the radiative formation of ship tracks. *J. Atmos. Sci.*, **57**, 2607-2624.

Twomey, S., 1974: Pollution and the planetary albedo. *Atmos. Environ.*, **8**, 1251-1256.

Wallace, J. M., and P. V. Hobbs, 1977: *Atmospheric science an introductory survey*, Academic Press, San Diego, California.

## **Appendix**

### **Automated Scheme for Identifying Ship Tracks**

The automated scheme for identifying pixels in which the clouds were polluted by underlying ships relied on the enhanced reflectances observed at near infrared wavelengths for the polluted clouds. The enhanced reflectances arise from the reduction in droplet radii. As was noted in Chapter 2, the identification of the polluted clouds and the nearby unpolluted clouds was a two-step process. First, the enhancement of near infrared reflectances was used to log the position of tracks by hand. The points were positioned at the head of the track, the location nearest the ship, and then at significant turns along the length of the track. Typically 5 to 10 points were located along a track, the longer tracks with more turns requiring more points.

Second, an automated algorithm was used to identify pixels that contained polluted clouds and then those on either side of the polluted pixels that served as unpolluted controls. The automated identification of the polluted pixels was designed to select pixels which had near infrared reflectances that stood well above the background reflectances exhibited by the neighboring pixels. The mean background reflectance was deduced as follows: first, the hand-logged track positions were used to align the analysis so that pixel distances were measured perpendicular to the track and the pixels were placed in rows that lay parallel to the track. The analysis was performed for short segments, typically 20 “pixels” in the along-track dimension with each segment typically 20 “pixels” on either side of the track in the cross-track dimension. Second, a linear least-squares fit was performed to determine the trend in

the near infrared reflectance as a function of pixel distance from the hand-located track center. The fit was applied to the pixels at the edges of the domain used to represent the background. The edge constituted all rows of pixels that fell within fifteen and twenty pixels of the hand-located track center. For each row of pixels, the pixel having the near infrared reflectance that was ranked fifth of the uppermost values was used in the least-square fit.

Figure A1 illustrates the procedure. It shows an isolated ship track imaged at  $2.1\ \mu\text{m}$ . The solid line in Fig. A1c shows the least-squares trend line for the  $2.1\text{-}\mu\text{m}$  reflectances in the boxed region of Figs. A1a and b. The pixels identified as containing polluted clouds were those that fell three standard deviations above the least-squares trend. These pixels are identified by + symbols in Fig. A1c.

Once the polluted pixels were identified for the entire length of the track, they were used to select the neighboring controls, pixels containing unpolluted clouds. Prior to identifying the unpolluted controls, the polluted pixels were scanned for any that were found to be unconnected to other polluted pixels. Such pixels were removed. While isolated clusters of adjacent pixels could represent a ship track, no isolated single pixel was allowed. After the removal of the isolated pixels, the control pixels were identified by shifting the pattern of the polluted pixels to either side of the track. Control pixels were chosen from the transported pattern but in a way that all of the selected pixels were at least one pixel away from any pixel identified as being polluted. As illustrated in Fig. A1b, the strategy leads to patterns in the controls that replicate those in the polluted pixels. Where the ship track is narrow, the patterns of the controls are narrow. Where the ship track is broad or its width is expanded as a

result of clusters of pixels being identified as polluted, the control pattern also expands. This procedure for duplicating the pattern of the polluted pixels was chosen so as to include in the controls any short-distance correlations that might exist among the cloud properties. The strategy was to select unpolluted control pixels that would replicate the polluted pixel pattern and lie as close to the polluted pixels as possible. The strategy was based on measurements of the autocorrelation lengths for cloud properties in overcast marine stratus, which were found to be less than 5 – 10 km, depending on the property, for 100-km scale regions containing homogeneous stratus systems. The strategy thus enhances the signal-to-noise ratio for determining the changes in cloud properties caused by the pollution against the natural variability of the marine stratocumulus.

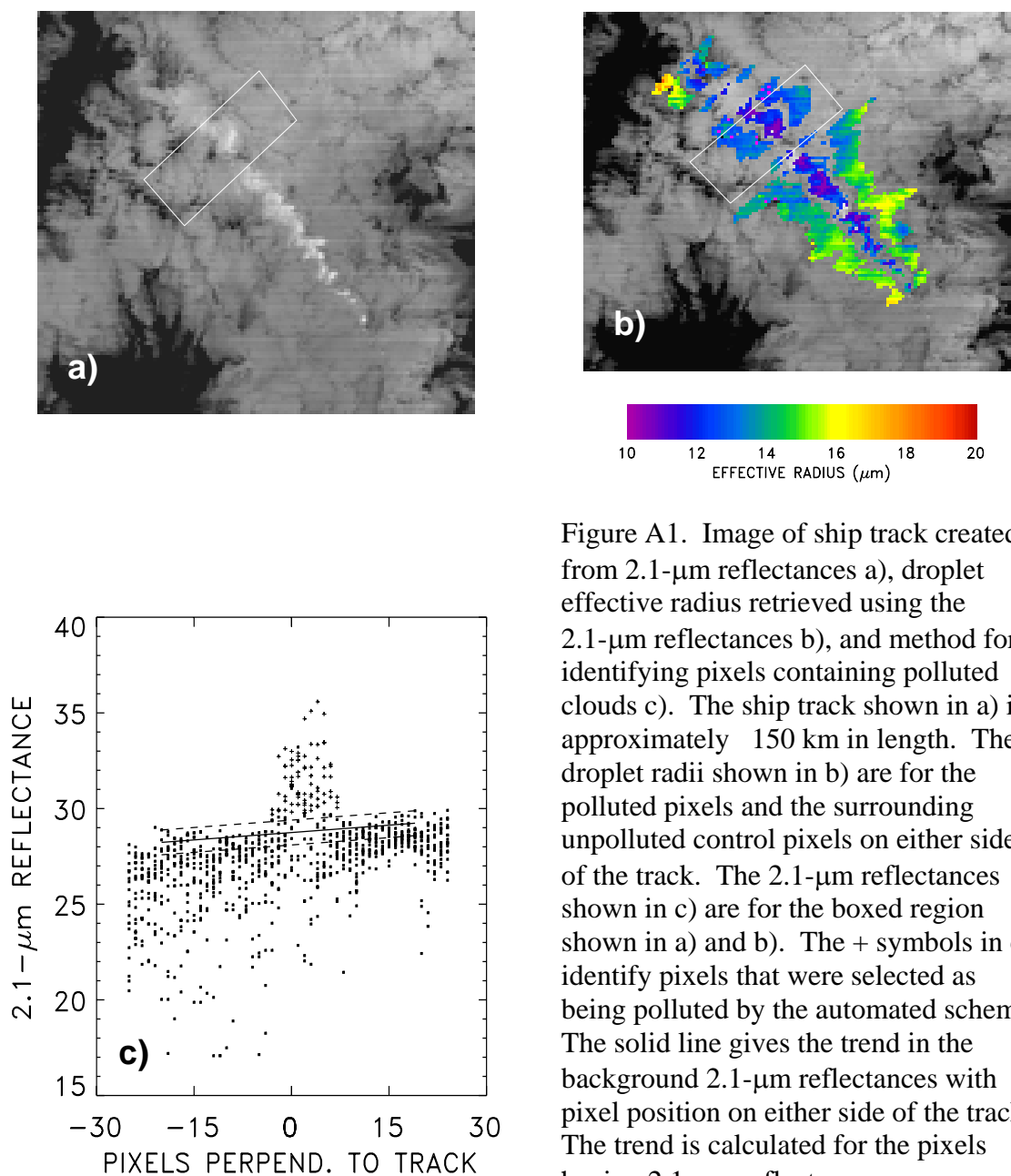


Figure A1. Image of ship track created from 2.1- $\mu\text{m}$  reflectances a), droplet effective radius retrieved using the 2.1- $\mu\text{m}$  reflectances b), and method for identifying pixels containing polluted clouds c). The ship track shown in a) is approximately 150 km in length. The droplet radii shown in b) are for the polluted pixels and the surrounding unpolluted control pixels on either side of the track. The 2.1- $\mu\text{m}$  reflectances shown in c) are for the boxed region shown in a) and b). The + symbols in c) identify pixels that were selected as being polluted by the automated scheme. The solid line gives the trend in the background 2.1- $\mu\text{m}$  reflectances with pixel position on either side of the track. The trend is calculated for the pixels having 2.1- $\mu\text{m}$  reflectances representative of the higher values for the background reflectances as discussed in the text. The dashed lines are displaced from the best fit trend by two standard deviations.